

1                   **Spatio-temporal control of DNA replication by the**  
2                   **pneumococcal cell cycle regulator CcrZ**

3

4 Clement Gallay<sup>1,#</sup>, Stefano Sanselicio<sup>1,#</sup>, Mary E. Anderson<sup>2</sup>, Young Min Soh<sup>1</sup>, Xue Liu<sup>1</sup>, Gro A.  
5 Stamsås<sup>3</sup>, Simone Pelliciani<sup>4</sup>, Renske van Raaphorst<sup>1</sup>, Julien Dénéréaz<sup>1</sup>, Morten Kjos<sup>3</sup>, Heath Murray<sup>4</sup>,  
6 Stephan Gruber<sup>1</sup>, Alan D. Grossman<sup>2</sup>, Jan-Willem Veening<sup>1,\*</sup>

7

8 <sup>1</sup> Department of Fundamental Microbiology, Faculty of Biology and Medicine, University of  
9 Lausanne, Biophore Building, CH-1015 Lausanne, Switzerland

10 <sup>2</sup> Department of Biology, Massachusetts Institute of Technology, Cambridge, MA, USA.

11 <sup>3</sup> Faculty of Chemistry, Biotechnology and Food Science, Norwegian University of Life Sciences, Ås,  
12 Norway

13 <sup>4</sup> Centre for Bacterial Cell Biology, Biosciences Institute, Newcastle University, Newcastle Upon  
14 Tyne NE2 4AX, UK

15

16 <sup>#</sup>These authors contributed equally

17 <sup>\*</sup>Correspondence to Jan-Willem Veening: [Jan-Willem.Veening@unil.ch](mailto:Jan-Willem.Veening@unil.ch), tel: +41 (0)21 6925625,

18 Twitter handle: @JWVeening

19

20 **Abstract**

21 Most bacteria replicate and segregate their DNA concomitantly while growing, before cell division  
22 takes place. How bacteria synchronize these different cell cycle events to ensure faithful chromosome  
23 inheritance is poorly understood. Here, we identified a conserved and essential protein in  
24 pneumococci and related Firmicutes named CcrZ (for Cell Cycle Regulator protein interacting with  
25 FtsZ) that couples cell division with DNA replication by controlling the activity of the master initiator  
26 of DNA replication, DnaA. The absence of CcrZ causes mis-timed and reduced initiation of DNA  
27 replication, which subsequently results in aberrant cell division. We show that CcrZ from  
28 *Streptococcus pneumoniae* directly interacts with the cytoskeleton protein FtsZ to place it in the  
29 middle of the newborn cell where the DnaA-bound origin is positioned. Together, this work uncovers  
30 a new mechanism for the control of the bacterial cell cycle in which CcrZ controls DnaA activity to  
31 ensure that the chromosome is replicated at the right time during the cell cycle.

32

33 **Main**

34 Most organisms have mechanisms ensuring that their genome is replicated and segregated prior to cell  
35 division. In many bacterial species, DNA replication and cell division occur concomitantly<sup>1,2,3</sup>.  
36 Different models emerged from the mid-1900's to explain how bacterial cells handle DNA replication  
37 together with cell division in *Escherichia coli* or *Bacillus subtilis*<sup>4,5,6,7</sup>. The current cell-size control  
38 model suggests that cells initiate DNA replication independently from their original size, and grow to  
39 a constant size independently from their size at birth (adder model)<sup>8,9,10,11,12</sup>. How cells sense changes  
40 in cell size and convert it to trigger replication initiation is not known, but these models imply the  
41 existence of regulatory controls<sup>3,13,14,15</sup>. However, no such cell cycle regulator has been reported yet  
42 for bacteria. Specific regulatory models have been proposed for *E. coli*<sup>16,17,18</sup>, but these are not  
43 applicable to most other organisms, and especially Gram-positive bacteria, that do not contain the  
44 proteins proposed to be the regulators. Furthermore, most of the mechanisms known to regulate the  
45 initiation of replication and the activity of the replication initiator DnaA in *E. coli* do not exist in other  
46 bacteria<sup>19,20,21,22,23</sup>. This pinpoints a divergence between regulatory systems within bacteria. In line  
47 with this notion, changes in DNA replication initiation were shown to alter cell size in *E. coli* and *B.*  
48 *subtilis* but the converse was not true for *B. subtilis*<sup>24,25</sup>. Taken together, current data indicates that  
49 bacteria evolved different mechanisms to coordinate their cell cycle events.

50         Although *E. coli* and *B. subtilis* use different systems for regulating their cell cycle, the way  
51 they localize their division site is conserved, as both organisms use a variant of the Min system to  
52 prevent polymerization of the tubulin-like protein FtsZ away from mid-cell<sup>26,27</sup>. Both species also  
53 have a nucleoid occlusion system (Noc) inhibiting Z-ring formation over the chromosome to prevent  
54 “cutting” of the chromosome during cell division<sup>28</sup>. Together, the Min and Noc systems ensure that  
55 cell division and septation occur when both sister chromatids have been fully replicated and  
56 segregated. These systems are however not conserved within all bacteria as the Gram-positive  
57 opportunistic human pathogen *S. pneumoniae* lacks homologs of the Min and Noc systems<sup>29</sup>. In  
58 contrast to *E. coli* and *B. subtilis*, the pneumococcal Z-ring forms readily over the nucleoid<sup>29,30</sup>.  
59 Recently, a pneumococcal specific protein called RocS was identified that might fulfil a similar

60 function as the Noc system by connecting chromosome segregation with capsule production<sup>31</sup>.  
61 Another *S. pneumoniae* specific protein, called MapZ was shown to guide Z-ring formation,  
62 analogous to the Min system in other bacteria<sup>32,33</sup>. During cell growth, nascent MapZ rings are pushed  
63 apart by septal peptidoglycan synthesis, allowing for FtsZ polymers to continuously assemble at the  
64 newly formed septum<sup>34</sup>. Importantly, the position of the origin of replication (*oriC*) was shown to be  
65 crucial for division site selection in *S. pneumoniae* and the origins mark the approximate positions of  
66 future division sites<sup>35</sup>. In *S. pneumoniae*, cell division and DNA replication are thus intimately  
67 connected. Critically however, it remains unknown how the cell senses when a new round of  
68 replication should be initiated.

69 We hypothesized that an unknown factor could be responsible for coordination of cell  
70 division and DNA replication in the pneumococcus. Using high throughput gene silencing with  
71 CRISPRi of all essential genes of *S. pneumoniae*<sup>36</sup>, we examined proteins leading to DNA content  
72 defects upon depletion. Here, we describe the identification of CcrZ, a conserved protein that activates  
73 DnaA to trigger initiation of DNA replication. Pneumococcal CcrZ localizes at the division site in a  
74 FtsZ-dependent manner and its inactivation leads to division defects. Together, our findings show that  
75 CcrZ acts as a novel spatio-temporal link between cell division and DNA replication in *S.*  
76 *pneumoniae*.

77

## 78 **CcrZ is a conserved bacterial cell cycle protein**

79 We previously generated a knock-down library using CRISPRi (clustered regularly interspaced short  
80 palindromic repeats interference) targeting 348 conditionally essential genes of the serotype 2 strain *S.*  
81 *pneumoniae* D39V that were identified by Tn-Seq (transposon-insertion sequencing)<sup>36</sup>. Here, we  
82 investigated the function of *spv\_0476*, encoding a protein of unknown function that is conserved in  
83 most Firmicutes (>30% identity) (Extended Data Fig. 1a). Silencing of *spv\_0476* by CRISPRi led to a  
84 drastic reduction of the growth rate as well as appearance of anucleate cells as visualized by DAPI  
85 staining (Fig. 1a,b). We renamed SPV\_0476 to CcrZ (for Cell Cycle Regulator protein interacting  
86 with FtsZ) for reasons explained below. *ccrZ* is in an operon with *trmB*, which encodes a tRNA  
87 methyltransferase and this operon structure is conserved across Firmicutes (Extended Data Fig. 1a).

88 To exclude the possibility that the observed phenotypes of *ccrZ* silencing were caused by polar effects  
89 on *trmB* expression, we constructed a deletion of *trmB*. This deletion did not lead to any growth defect  
90 (Extended Data Fig. 1b left panel). While Tn-seq indicated that *ccrZ* is essential<sup>36</sup>, we were able to  
91 generate a  $\Delta ccrZ$  deletion mutant, although cells grew very slowly. We therefore constructed a  
92 depletion of CcrZ by ectopically expressing CcrZ under control of either an IPTG- or a ZnCl<sub>2</sub>-  
93 inducible promoter ( $P_{lac}$  and  $P_{Zn}$  respectively) and deleted *ccrZ* from its native location ( $ccrZ^{+/+}$  and  
94  $P_{Zn}\text{-}ccrZ^{+/+}$  respectively). Depletion of CcrZ led to a significant growth delay at 37°C and 30°C,  
95 confirming the CRISPRi observations (Extended Data Fig. 1b). Immunoblotting using a specific  
96 antibody raised against purified CcrZ confirmed CcrZ depletion (Extended Data Fig. 1c).

97 In line with the CRISPRi observations, DNA staining of cells depleted for CcrZ showed that  
98 20% of cells lacked a nucleoid (Fig. 1c, 442 cells counted). To test whether the *ccrZ*-deletion  
99 phenotype was conserved in other Gram-positive bacteria, we silenced *ccrZ* (*SAOUHSC\_01866*, here  
100 *ccrZ<sub>Sa</sub>*) in *Staphylococcus aureus* SH1000 using CRISPRi and deleted the *Bacillus subtilis* 168 *ccrZ*  
101 homolog (*ytmP*, here *ccrZ<sub>Bs</sub>*). Upon *ccrZ<sub>Sa</sub>* silencing in *S. aureus*, we observed a high proportion of  
102 anucleate cells, as well as a delay in growth. In contrast, no anucleate cells were observed for *B.*  
103 *subtilis* (Extended Data Fig. 1d). However, cells deleted for *ccrZ<sub>Bs</sub>* were slightly thinner and longer  
104 although they grew with a growth rate similar to the wild type (Extended Data Fig. 1d). Interestingly,  
105 the *S. pneumoniae* *ccrZ* deletion could not be complemented by expression of *ccrZ* from either *B.*  
106 *subtilis* or *S. aureus* as only very small colonies were present on agar plates. In contrast, depletion of  
107 *S. aureus* CcrZ was rescued by expression of CcrZ from *B. subtilis* (Extended Data Fig. 1d).

108 In addition to an increase of the number of anucleate cells, CcrZ depletion in *S. pneumoniae*  
109 also led to slight morphological defects and modest changes in cell size when analyzed by phase  
110 contrast microscopy (slight decrease in length and increase in width) (Fig. 1d). Polysaccharide capsule  
111 production has previously been linked to the pneumococcal cell cycle<sup>37</sup>, but capsule production was  
112 not impacted as the amount of capsule was similar between a CcrZ mutant and wild type (Extended  
113 Data Fig. 1e). To visualize division sites in live cells, we constructed a translational fusion of  
114 mTurquoise2 to FtsZ (as the only copy of FtsZ, expressed from its native genetic location), which  
115 assembles into distinct rings at new division sites where it recruits the machinery required to form

116 septa<sup>38</sup>. As shown in Figure 1e, Z-rings were clearly mis-localized upon CcrZ depletion for 3h, with  
117 the presence of several aberrant Z-rings in 43% of the cells (Fig. 1e). To obtain more insights into the  
118 morphological defects caused by CcrZ depletion and verify that the increased number of septa are not  
119 due to the fluorescent protein fused to FtsZ, we employed transmission electron microscopy (TEM) in  
120 untagged cells. While not evident by phase contrast microscopy, when *ccrZ* was depleted we observed  
121 frequent aberrant septum formation using TEM, in line with the FtsZ localization data, and many cells  
122 harbored two (18 %) to four (4 %) septa while only one septum is observed in 91% of wild type cells  
123 (Fig. 1f,g).

124

### 125 *S. pneumoniae* CcrZ is part of the divisome

126 As CcrZ seems to be involved in both chromosome biology and cell division, we examined its  
127 subcellular localization. Strikingly, immunofluorescence on fixed cells using a CcrZ-specific antibody  
128 demonstrated a clear mid-cell localization (Extended Data Fig. 2a). To assess the localization of CcrZ  
129 in live cells, we created several functional fusions of a green fluorescent protein to the N-terminus of  
130 CcrZ (*gfp-ccrZ*) or a red fluorescent protein to the C-terminus (*ccrZ-mKate2*) and inserted either  
131 construct at the native *ccrZ* locus (Extended Data Fig. 1c). Visualization of fluorescently tagged CcrZ  
132 by epifluorescence microscopy in live bacteria showed that CcrZ localizes at mid-cell (Fig. 2a). This  
133 localization was also conserved in both the TIGR4 and unencapsulated R6 strains (Extended Data Fig.  
134 2b). Interestingly, CcrZ<sub>Sa</sub> and CcrZ<sub>Bs</sub> did not localize as clear rings at mid-cell in *S. aureus* and *B.*  
135 *subtilis* (Extended Data Fig. 2b), indicating that the activity and/or localization of CcrZ in these  
136 organisms is regulated differently. In order to get higher spatial resolution of *S. pneumoniae* CcrZ,  
137 240 images (16 stacks) on live cells were acquired using 3D-structured illumination microscopy (3D-  
138 SIM) and reconstructed to generate a super resolution image and a 3D fluorescence image of GFP-  
139 CcrZ. As shown in Fig. 2b and Supplementary Video 1, CcrZ forms a patchy ring at mid-cell.  
140 Furthermore, time-lapse microscopy showed that CcrZ disassembles from the old septum to assemble  
141 at the newly formed division site (Supplementary Video 2).

142 To test whether the mid-cell localization of *S. pneumoniae* CcrZ coincides with FtsZ, we  
143 constructed a CcrZ / FtsZ double-labelled strain (*gfp-ccrZ ftsZ-mCherry*). As shown in Fig. 2c, CcrZ

144 co-localized with FtsZ and analysis of still images from exponentially growing cells corroborated this  
145 observation (Fig. 2c-e and Supplementary Video 3). Note that the FtsZ-mCherry fusion did affect the  
146 growth or morphology of the cells<sup>39</sup>. 3D-SIM also indicated an overlap of GFP-CcrZ and FtsZ-  
147 mCherry as well as a similar circular co-localizing pattern at mid-cell (Fig. 2f, Extended Data Fig. 2c  
148 and Supplementary Video 4).

149 Prediction of CcrZ's topology using TMHMM<sup>40</sup> did not indicate the presence of a  
150 transmembrane domain; CcrZ's septal localization might then rely on another partner. To identify  
151 possible partners, we purified GFP-CcrZ expressed from *S. pneumoniae* and untagged cytosolic  
152 sfGFP as a control using anti-GFP nanobodies (GFP-Trap) without cross-linking, and directly  
153 analyzed the purified fraction by liquid chromatography-tandem mass spectrometry (LC-MS/MS).  
154 Interestingly, we found an enrichment (> 5-fold change) for several proteins from the divisome (e.g.,  
155 FtsZ, PBP2X and EzrA) (Supplementary Table 3). To determine which of the candidates might  
156 interact directly with CcrZ, we used the NanoBit complementation reporter assay<sup>41,42</sup>, which uses an  
157 enhanced luciferase separated into two different fragments (large bit (LgBit) and small bit (SmBit),  
158 respectively). Fusion of two different interacting proteins to each fragment can restore the activity of  
159 the luciferase and, in presence of a furimazine-based substrate, produce light<sup>41</sup>. Accordingly, we fused  
160 the C-terminal extremity of CcrZ to LgBit (*ccrZ-LgBit*) and putative partners to SmBit and integrated  
161 the different constructs at their respective loci under native control. We also fused SmBit to other  
162 proteins known to localize at the septum (Cps2E, FtsA, FtsW and ZapA), or to the highly abundant  
163 histone-like protein HlpA localizing at the nucleoid and used a strain expressing both HlpA-LgBit and  
164 HlpA-SmBit as a positive control of interaction. After addition of the substrate, we could detect a  
165 strong and reproducible signal when FtsZ was fused to SmBit and CcrZ to LgBit, as well as a weaker  
166 signal for FtsA, EzrA and ZapA, and no detectable signal for any of the other proteins (Fig. 3a). This  
167 result indicates that FtsZ and CcrZ in *S. pneumoniae* are in very close proximity in space.  
168 Interestingly, using a strain expressing both CcrZ-LgBit and CcrZ-SmBit, a weak signal was observed  
169 indicating that CcrZ might also self-interact (Fig. 3a).

170 To confirm the observed interaction with FtsZ, we used a bacterial two-hybrid assay in *E.*  
171 *coli*<sup>43</sup>. Again, we observed a robust interaction between CcrZ and FtsZ, while T25-FtsZ did not

172 interact with the empty vector alone, strongly suggesting that CcrZ directly binds to FtsZ (Fig. 3b).  
173 Co-immunoprecipitation of FtsZ-GFP from *S. pneumoniae* cells confirmed the *in vivo* interaction with  
174 CcrZ (Fig. 3c). Affinity purification of CcrZ<sub>Sp</sub>-GFP when over-expressing FtsZ<sub>Sp</sub> in *E. coli* also  
175 confirmed this interaction as we were able to co-purify FtsZ in large amounts (Fig. 3d). To test  
176 whether the localization of CcrZ depends on FtsZ, we constructed a strain expressing CcrZ-mKate2 as  
177 well as a second copy of FtsZ under the control of an IPTG-inducible promoter and deleted the native  
178 *ftsZ* gene (*ftsZ*<sup>+</sup>). As expected, FtsZ depletion led to aberrant cell morphology and, consistent with a  
179 FtsZ-CcrZ interaction, CcrZ-mKate2 was rapidly mis-localized and the signal was spread throughout  
180 the cytoplasm (Fig. 3e and Supplementary Video 5). In total, we conclude that CcrZ localizes to new  
181 division sites via a direct interaction with FtsZ.

182

### 183 **CcrZ controls DNA replication**

184 As shown in Fig. 1c, when cells are depleted for CcrZ, a large proportion of cells become anucleate.  
185 To investigate the consequences of lack of CcrZ on chromosome segregation in live cells, we  
186 introduced a translational fluorescent fusion of HlpA<sup>44</sup> and deleted *ccrZ*. Localization of HlpA-  
187 mKate2 in this slow growing  $\Delta ccrZ$  mutant showed similar results to DAPI stained cells depleted for  
188 CcrZ and we observed that 19 % of cells lacked a nucleoid signal (Extended Data Fig. 3a, 4855 cells  
189 counted). Time-lapse imaging indicated that cells with defective DNA content had either no DNA at  
190 all or chromosomes “guillotined” during septum closure suggesting reduced nucleoid occlusion  
191 control in  $\Delta ccrZ$  (Fig. 4a and Supplementary Video 6). We also co-localized FtsZ-CFP with HlpA-  
192 mKate2 while depleting CcrZ for a short period of time (2h). Interestingly, we observed many cells  
193 with a chromosome localized at only one half of the cell, at one side of the Z-ring (Fig. 4b). The  
194 absence of DNA in the other half of the cell could be explained by defective DNA segregation, by  
195 impaired replication or by DNA degradation.

196 When attempting to make clean *ccrZ* deletions, in addition to small colonies typical of slow  
197 growing mutants, there were also spontaneous large, wild type-sized colonies. Growth analysis of  
198 cells from three of these large colonies (*ccrZ*<sup>supp1-3</sup>) showed that cells behaved like wild type and



199 DAPI staining revealed a restoration of wild type DNA content (Fig. 4c,d). To verify whether these  
200 wild type-like phenotypes were caused by suppressor mutations, the genomes of these fast-growing  
201 strains were sequenced. All three strains still contained the *ccrZ* deletion and, in addition, contained a  
202 single nucleotide polymorphism elsewhere in the genome (Fig. 4e). Two missense mutations were  
203 found in *dnaA* (DnaA-Q247H and DnaA-S292G) and one nonsense mutation in *yabA* (YabA-E93\*<sup>3</sup>).  
204 Since DnaA promotes initiation of DNA replication and YabA hampers it by preventing interaction of  
205 DnaA with DnaN<sup>45</sup>, we wondered whether the frequency of DNA replication initiation was changed  
206 in a *ccrZ* mutant.

207 To test this hypothesis, we quantified the copy number ratio between chromosomal origin and  
208 terminus regions (*oriC/ter* ratios) using real-time quantitative PCR. In a wild type situation, during  
209 exponential growth, the *oriC/ter* ratio varies between 1.3 – 1.8, as most cells have started a round of  
210 DNA replication (note that in contrast to *E. coli* and *B. subtilis*, multifork replication does not occur in  
211 *S. pneumoniae*)<sup>46</sup>. Remarkably, depletion of CcrZ resulted in a significantly decreased DNA  
212 replication initiation rate with an *oriC/ter* ratio of 1.1 vs 1.8 for complemented cells (*P* value < 0.05)  
213 (Fig. 4f). Interestingly, the same observation was made for both *B. subtilis* and *S. aureus*, where  
214 deletion or depletion of CcrZ caused a clear reduction in *oriC/ter* ratios (Fig. 4g). As the identified  
215 *ccrZ*-bypass mutations were found in DNA replication initiation regulators, we tested whether they  
216 would restore the *oriC/ter* ratio in a fresh *ccrZ* deletion background in *S. pneumoniae*. Indeed, the  
217 *oriC/ter* ratios for  $\Delta ccrZ$  *dnaA-S292G*,  $\Delta ccrZ$  *dnaA-Q247H* and for *yabA-E93\** (*ccrZ*<sup>supp3</sup>) were like  
218 wild type (Fig. 4h,i).

219 The point mutation found in *yabA* causes premature translation termination at the C-terminus  
220 of YabA. When *yabA* alone was replaced by an antibiotic resistance cassette, we observed an increase  
221 of replication initiation as well as a reduced growth rate; but when *ccrZ* was co-deleted, wild type like  
222 growth and a wild type *oriC/ter* ratio was restored (Fig. 4i,j). DnaA suppressor mutations were  
223 located in the AAA+ ATPase domain of DnaA<sup>47</sup> (Extended Data Fig. 3b) and it was previously  
224 reported that specific mutations in this domain could increase the initiation rate in *B. subtilis*<sup>48</sup>. To  
225 determine if those mutations alone were able to induce over-initiation, we inserted each *dnaA*  
226 mutation into a wild type background strain. Marker frequency analysis detected an increase in the

227 *oriC/ter* ratio for both *dnaA* alleles (Fig. 4k). We conclude that mutations that increase the rate of  
228 initiation of DNA replication can rescue the  $\Delta ccrZ$  phenotype.

229 To gain additional insights into CcrZ function, we performed a genome-wide genetic  
230 interaction screen in cells depleted for CcrZ using CRISPRi-seq<sup>49</sup> (Fig. 4l). This technique relies on  
231 the expression of dCas9, controlled by an anhydrotetracycline (aTc) -inducible promoter, and  
232 constitutive expression of a specific sgRNAs that together form a roadblock for RNAP and thereby  
233 downregulated transcription of the targeted operon. We created a CRISPRi library by transforming *S.*  
234 *pneumoniae*  $P_{ter}$ -dCas9,  $P_{lac}$ -*ccrZ*,  $\Delta ccrZ$  with 1,499 different sgRNAs targeting 2,111 out of 2,146  
235 genetic elements of *S. pneumoniae*. The resulting library was grown in presence or absence of aTc to  
236 repress, or not, every operon, and in presence or absence of IPTG to express or deplete *ccrZ*, and the  
237 sgRNAs were then sequenced by Illumina sequencing. If an operon becomes more essential in a *ccrZ*-  
238 depletion background than in an induced *ccrZ* background, the corresponding sgRNA will therefore  
239 be under-represented. After analyzing the fold change for every sgRNA between *ccrZ*-depletion and  
240 *ccrZ*-complementation, we found an enrichment of sgRNAs targeting the operon of YabA / HolB  
241 (*tmk-holB-yabA-spy\_0828*), indicating that depletion of this operon becomes beneficial for growth of  
242  $\Delta ccrZ$  (Fig. 4m and Supplementary Table 4). This confirms that deletion of YabA can complement a  
243 *ccrZ* deletion. Interestingly, we also found that inactivation of two genes coding for FtsK and RocS,  
244 worsened the fitness of a *ccrZ* mutant. RocS is a regulator of chromosome segregation in *S.*  
245 *pneumoniae* interacting with the DNA and the chromosome partitioning protein ParB<sup>50</sup> and FtsK is  
246 thought to couple segregation of the chromosome terminus during cell division<sup>51</sup>. These interactions  
247 reinforce a role of CcrZ in chromosome integrity and replication and that CcrZ acts in a distinct  
248 pathway from these chromosome segregation factors. Finally, to test whether the midcell localization  
249 of CcrZ is important for well-timed replication of the chromosome, we abrogated CcrZ's mid-cell  
250 localization by depleting cells for FtsZ (Fig. 3e). After 2h of FtsZ depletion, chromosomal DNA was  
251 isolated and *oriC/ter* ratios were determined. This showed that upon mis-localization of CcrZ, cells  
252 under replicate (Fig. 4n).

253

254 **CcrZ is a conserved regulator of DnaA**

255 The results so far suggest that the division defects observed in the absence of CcrZ are due to  
256 perturbed Z-ring formation caused by under-replication of the chromosome. To examine whether  
257 disruption of DNA replication in general could lead to division defects similar to those of a *ccrZ*  
258 mutant, we took advantage of a thermosensitive *dnaA* mutant (*dnaA<sup>TS</sup>*) in which DNA replication  
259 initiation is drastically reduced when cells are grown at the non-permissive temperature (40°C)<sup>50</sup>. As  
260 expected, when shifted to the non-permissive temperature, many cells were anucleate (Extended Data  
261 Fig. 4a). Strikingly, localization of FtsZ-mTurquoise2 in the *dnaA<sup>TS</sup>* strain at 40°C phenocopied the  
262  $\Delta$ *ccrZ* mutant, and FtsZ was frequently mis-localized (Fig. 5a). Examination by time-lapse  
263 microscopy following a temperature shift from 30°C to 40°C showed that FtsZ-mTurquoise2 mis-  
264 localization occurs after four to five generations (Supplementary Video 7). Furthermore, examination  
265 by TEM at 40°C showed many cells with aberrant septa like CcrZ-depleted cells (Fig. 5b). As DnaA  
266 inactivation leads to strikingly similar phenotypes, these data are consistent with the idea that CcrZ  
267 exerts a control on DNA replication initiation.

268 To test whether CcrZ controls DNA replication via regulating DnaA activity, we made use of  
269 the fact that a *B. subtilis*  $\Delta$ *ccrZ<sub>Bs</sub>* mutant also under-initiates (Fig. 4g) and a strain was constructed in  
270 which DNA replication was driven in a RepN-dependent manner (from a plasmid origin of replication  
271 *oriN*) rather than from DnaA-dependent initiation (from *oriC*). This showed no significant *ori-ter*  
272 ratio differences when *ccrZ* was deleted (Fig. 5c), suggesting that CcrZ is an activator of DnaA-  
273 dependent initiation of replication in *B. subtilis*. We therefore tested whether CcrZ interacts directly  
274 with DnaA to trigger DNA replication and employed bacterial two-hybrid assays and the Split-luc  
275 system using pneumococcal CcrZ and DnaA (Fig. 3a and Extended Data Fig. 4b). However, none of  
276 these assays revealed a direct protein-protein interaction. In line with our genetic data, we also did not  
277 find a direct interaction of CcrZ with YabA, while YabA clearly interacts with DnaA (Extended Data  
278 Fig. 4c). It is still possible that CcrZ interacts directly with DnaA, but that we cannot detect it with  
279 these assays. Alternatively, another factor might be required for CcrZ's function or CcrZ indirectly  
280 affects the activity of DnaA in replication initiation.

281

282 **CcrZ's conserved residues are essential for its function**

283 *S. pneumoniae* CcrZ is 264 amino acids long and is predicted to have a single APH (aminoglycoside  
284 phosphotransferase enzyme family) domain (Fig. 5d). Sequence alignment using Psi-BLAST showed  
285 homology with phosphotransferase enzyme family proteins, while pairwise comparisons of profile-  
286 hidden Markov models (HMMs) using HHpred<sup>52</sup> identified homologies with ethanolamine- and  
287 choline kinases. Despite various attempts, we have not been able to establish any biochemical activity  
288 or nucleotide binding for recombinant purified CcrZ and were unable to produce protein crystals,  
289 probably because of its rapid precipitation in solution. Nevertheless, as CcrZ is highly conserved in  
290 Firmicutes, we aligned CcrZ protein sequence with 1000 protein sequences from UniRef50 and  
291 identified three residues conserved in more than 95% of the proteins (D159, N164 and D177) and two  
292 other residues (H157 and D189) in more than 80% (Fig. 5d and Extended Data Fig. 4d). To determine  
293 the position of these residues, the *S. pneumoniae* CcrZ protein sequence was mapped onto the crystal  
294 structure of the best hit from the HMM alignment, the choline kinase LicA, in complex with  
295 adenosine monophosphate (AMP) (pdb 4R78). Interestingly, these five conserved residues appear to  
296 be in spatial proximity to AMP and thus to a putative nucleotide-binding pocket (Fig. 5e).  
297 Comparison of CcrZ and LicA sequences shows a conserved Brenner's motif [HXDhX3N] (residues  
298 CcrZ H157 – N164) found in most phosphotransferases (Fig. 5d). In this motif, LicA-N187 (CcrZ-  
299 N164) was shown to interact with the  $\alpha$ -phosphate moiety of AMP<sup>53</sup> and LicA-D176 (CcrZ-D159)  
300 was shown to be crucial for hydrogen bond formation with the hydroxyl moiety of choline.  
301 Furthermore, it also has a conserved motif found in phosphotransferases (APH), in which LicA-  
302 D194 (CcrZ-D177) was shown to interact with the  $\alpha$ -phosphate moiety of AMP. CcrZ-D189  
303 corresponds to residue D313 of the choline kinase A (cka-2) of *Caenorhabditis elegans*, a residue  
304 which was proposed to stabilize the cka-2 dimer as well as the catalytic site<sup>54</sup>. CcrZ however does not  
305 possess the conserved hydrophobic residues specific to choline- and ethanolamine-kinases necessary  
306 for choline binding, but instead has several polar amino acids at these positions (e.g., the crucial  
307 residues LicA-Y197 and V178 corresponding to CcrZ-S180 and R161). Mutational analysis of the  
308 five conserved residues of CcrZ showed that at least H157, N164 and D177 are essential for CcrZ's  
309 function in *S. pneumoniae* (Fig. 5f), while mutating CcrZ-D159 or CcrZ-D189 did not lead to any  
310 growth defect. All three essential mutants were properly produced (Extended Data Fig. 1c) and CcrZ-

311 H157A and CcrZ-D177A could still localize at the septum (Fig. 5g). Therefore, these three residues  
312 are crucial for the function of CcrZ. It is interesting to note that none of the three mutants was  
313 dominant negative when expressed together with a wild type CcrZ. Given the high similarity with  
314 LicA, it is very likely that CcrZ can bind an as of yet unknown nucleotide.

315

### 316 **A model for CcrZ-controlled DNA replication in *S. pneumoniae***

317 We showed above that CcrZ is fundamental for DnaA-dependent DNA replication initiation in *B.*  
318 *subtilis* and that *S. pneumoniae* CcrZ localizes at mid-cell for most of the cell cycle. In *S. pneumoniae*,  
319 once DNA replication initiates at mid-cell, the origins localize at both future division sites, while the  
320 replication machinery stays near the Z-ring until completion of replication and closure of the  
321 septum<sup>35</sup>. We therefore hypothesized that CcrZ is brought to mid-cell by FtsZ to promote initiation of  
322 DNA replication. To map the hierarchy of events that take place during the pneumococcal cell cycle,  
323 we constructed a triple-labeled strain (strain *ccrZ-mKate2 dnaN-sfTQ<sup>OX</sup> parB<sub>p</sub>-mYFP*) in which CcrZ  
324 is fused to a red fluorescent protein, DNA replication is visualized by a DnaN fusion to a cyan  
325 fluorescent protein, and the origin of replication is marked with a yellow fluorescent reporter (see  
326 Methods). Imaging of this strain by short time-lapse fluorescence microscopy revealed that DNA  
327 replication initiates once CcrZ is assembled at mid-cell, rapidly followed by segregation of the newly  
328 replicated origins as cells elongate (Fig. 6a-d and Supplementary Video 8). The replication machinery  
329 remains near the old division site together with CcrZ, only to move to the new cell division sites once  
330 DNA replication is complete. This data supports a model in which FtsZ brings CcrZ to *oriC* to  
331 stimulate DnaA to fire a new round of replication ensuring that DNA replication only commences  
332 after the origins are well segregated and positioned at the new mid-cell position. Indeed, DnaA co-  
333 localizes with CcrZ in new-born cells (Extended Data Fig. 5). In the absence of CcrZ, initiation of  
334 DNA replication is mis-timed and occurs too late relative to cellular growth and Z-ring formation,  
335 frequently leading to futile division events, mis-segregated chromosomes and anucleate cells (Fig.  
336 6e).

337

### 338 **Discussion**

339 The principal contribution of this work is the identification and initial functional characterization of a  
340 new mechanism for cell cycle regulation in *S. pneumoniae* via the CcrZ protein. We show that CcrZ's  
341 septal localization occurs via a direct interaction with FtsZ. Our data is consistent with a model in  
342 which, once positioned at mid-cell where the DnaA-bound origin of replication is located, CcrZ  
343 stimulates DnaA, likely by phosphorylation of an intermediate molecule, to initiate DNA replication  
344 (Fig. 6). Importantly, CcrZ's function of controlling DnaA seems conserved in *S. aureus* and *B.*  
345 *subtilis*, and likely in many other Gram-positive bacteria (Extended data Fig. 1a).

346 Besides the production of anucleate cells and cells with cleaved chromosomes, *ccrZ* mutants  
347 contain multiple aberrant division septa (Fig. 6e). Notably, this is phenocopied by a temperature  
348 sensitive DnaA allele. This indicates that chromosome replication itself, and correct localization of the  
349 chromosome has an important role in nucleoid occlusion: when initiation is too late and the new  
350 daughter chromosomes are not fully segregated, division can take place over the DNA resulting in  
351 dissected chromosomes. We also observed multiple division septa in cells depleted for CcrZ that are  
352 likely caused by mis-timed chromosome segregation whereby Z-rings are formed adjacent to the  
353 nucleoid. These phenotypes are reminiscent of observations made for *E. coli* and *B. subtilis* that  
354 showed that after arrest of DNA replication, many cells continued to elongate without dividing, but  
355 FtsZ rings continued to form and almost always were located to the side of nucleoids<sup>55,56</sup>. In this  
356 respect, it is interesting to note that the *S. aureus* Noc system also controls DNA replication, as  $\Delta noc$   
357 cells over-initiate DNA replication<sup>57</sup>. In support of our findings, a lethal  $\Delta noc \Delta comEB$  double mutant  
358 in *S. aureus* could be rescued by a suppressor mutation in *ccrZ*<sub>Sa</sub><sup>57</sup>, further indicating that CcrZ<sub>Sa</sub> is  
359 also involved in the control of DNA replication in *S. aureus*.

360 This work uncovers a novel mechanism in which a single protein links cell division with  
361 DNA replication control. In this model, Z-ring formation is used as a timer for the initiation of DNA  
362 replication. When cell division terminates, leading to the formation of another Z-ring at the new  
363 division site, CcrZ is brought along and can activate a new round of DNA replication. This simple  
364 system ensures that DNA replication only commences a single time per cell cycle in newborn cells. It  
365 will be interesting to see how CcrZ controls the cell cycle in other bacteria, what the involved  
366 biochemical activities are and whether CcrZ will prove as a new target for innovative antibiotics.



368 **Methods**

369 **Bacterial strains and culture conditions.**

370 All strains, plasmids and primers used are listed in Supplementary Table 1 and Supplementary Table  
371 2.

372 All pneumococcal strains in this study are derivate of *S. pneumoniae* D39V<sup>58</sup>, unless specified  
373 otherwise, and are listed in Supplementary Table 1. Strains were grown in liquid semi-defined C+Y  
374 medium<sup>59</sup> at 37°C from a starting optical density (OD<sub>600nm</sub>) of 0.01 until the appropriate OD. Induction  
375 of the zinc-inducible promoter (*P<sub>Zn</sub>*) was carried out by supplementing the medium with 0.1 mM  
376 ZnCl<sub>2</sub> and 0.01 mM MnCl<sub>2</sub> (Sigma-Aldrich) and the IPTG-inducible promoter (*P<sub>lac</sub>*) was activated  
377 with 1 mM IPTG (β-D-1-thiogalactopyranoside, Sigma-Aldrich). For all related experiments,  
378 depletion strains were first grown without inducer until OD<sub>600nm</sub> = 0.3 and then diluted 100 times in  
379 fresh medium and grown until the desired OD. Transformation of *S. pneumoniae* was performed as  
380 described before<sup>59</sup> with cells taken at exponential growth phase (OD<sub>600nm</sub> = 0.1). When necessary, the  
381 medium was supplemented with the following antibiotics: chloramphenicol (0.45 μg.mL<sup>-1</sup>),  
382 erythromycin (0.2 μg.mL<sup>-1</sup>), kanamycin (250 μg.mL<sup>-1</sup>), spectinomycin (200 μg.mL<sup>-1</sup>) and tetracycline  
383 (0.5 μg.mL<sup>-1</sup>).

384 *S. aureus* strains are listed in Supplementary Table 1. Cells were grown in brain heart infusion  
385 (BHI) medium (Oxoid) with shaking at 37°C. When appropriate, 5 μg.mL<sup>-1</sup> erythromycin and / or 10  
386 μg.mL<sup>-1</sup> chloramphenicol was added to the growth medium. All *S. aureus* plasmids were initially  
387 made in *E. coli* strain IM08B<sup>60</sup>. *E. coli* IM08B was grown in LB medium at 37°C with shaking; 100  
388 μg.mL<sup>-1</sup> ampicillin was added when appropriate. Plasmids were then transformed into *S. aureus* by  
389 electroporation, as described previously<sup>61</sup>.

390 *B. subtilis* strains are listed in Supplementary Table 1. Cells were grown with shaking at 37°C  
391 in Luria-Bertani (LB) medium or S7 defined minimal medium with MOPS (3-(N-morpholino)  
392 propanesulfonic acid) buffer at a concentration of 50 mM rather than 100 mM supplemented with 1 %  
393 glucose, 0.1 % glutamate, trace metals, 40 μg.mL<sup>-1</sup> phenylalanine, and 40 μg.mL<sup>-1</sup> tryptophan<sup>62</sup>.



394 Standard concentrations of antibiotics were used when appropriate. *B. subtilis* strains were derived  
395 from 1A700 or JH642 (*pheA1 trpC2*)<sup>63</sup>.

396

### 397 **Strain construction**

398 Construction of strains is described in the Supplementary Methods.

399

### 400 **Microtiter plate-based growth assay**

401 For *S. pneumoniae* growth assays, cells were first grown in C+Y medium pH = 7.4 until mid-  
402 exponential growth phase ( $OD_{595nm} = 0.3$ ) with no inducer at 37°C, after which they were diluted 100  
403 times in fresh C+Y medium supplemented with IPTG or ZnCl<sub>2</sub> when appropriate. Cellular growth was  
404 then monitored every 10 min at either 37°C or 30°C in a microtiter plate reader (TECAN Infinite  
405 F200 Pro). Each growth assay was performed in triplicate. The lowest  $OD_{595nm}$  of each growth curve  
406 was normalized to 0.004 (detection limit of the reader and initial  $OD_{595nm}$  of the inoculum) and the  
407 average of the triplicate values were plotted, with the SEM (Standard Error of the Mean) represented  
408 by an area around the curve.

409 For assessment of *S. aureus* growth, CRISPRi knockdown strains were grown overnight in  
410 BHI medium. Cultures were then diluted 100-fold and grown until  $OD_{600nm} = 0.4$ . The cultures were  
411 then re-diluted 200-fold in medium with or without inducer 500 μM IPTG. Growth analysis was  
412 performed on a Synergy H1 Hybrid (BioTek) microtiter plate reader at 37°C with measurement of  
413  $OD_{600nm}$  every 10 min. Average of the triplicate values were plotted, with the SEM (Standard Error of  
414 the Mean) represented by an area around the curve.

415

### 416 **Phase contrast and fluorescence microscopy**

417 *S. pneumoniae* cells were grown in C+Y medium pH = 7.4 at 37°C to an  $OD_{595nm} = 0.1$  without any  
418 inducer and diluted 100 times in fresh C+Y medium supplemented when appropriate with IPTG (for  
419 activation of dCas9, complementation of CcrZ and FtsZ, or expression of fluorescent fusions) or  
420 ZnCl<sub>2</sub> (for CcrZ complementation or expression of fluorescent fusions). At  $OD_{595nm} = 0.1$ , 1 mL of  
421 culture was harvested by centrifugation 1 min at 9,000 x g. For DAPI staining, 1 μg.mL<sup>-1</sup> DAPI

422 (Sigma-Aldrich) was added to the cells and incubated for 5 min at room temperature prior to  
423 centrifugation. For imaging of bulk exponentially growing cultures, cells were washed twice with 1  
424 mL ice-cold PBS and re-suspended into 50  $\mu$ L ice-cold PBS; for time-lapse microscopy, cells were  
425 washed and re-suspended into 1 mL of fresh pre-warmed C+Y medium. 1  $\mu$ L of cells were then  
426 spotted onto PBS- or C+Y-polyacrylamide (10 %) pads. For time-lapse microscopy, pads were  
427 incubated twice for 30 min in fresh C+Y medium at 37°C prior to spotting. Pads were then placed  
428 inside a gene frame (Thermo Fisher Scientific) and sealed with a cover glass as described before<sup>64</sup>.  
429 Microscopy acquisition was performed either using a Leica DMI8 microscope with a sCMOS  
430 DFC9000 (Leica) camera and a SOLA light engine (Lumencor), or using a DV Elite microscope (GE  
431 Healthcare) with a sCMOS (PCO-edge) camera and a DV Trulight solid state illumination module  
432 (GE Healthcare), and a 100x/1.40 oil-immersion objective. Phase contrast images were acquired using  
433 transmission light (100 ms exposure). Still fluorescence images were usually acquired with 700 ms  
434 exposure, and time-lapses with 200-300 ms exposure. Leica DMI8 filters set used are as followed:  
435 DAPI (Leica 11533333, Ex: 395/25 nm, BS: LP 425 nm, Em: BP 460/50 nm), CFP (Ex: 430/24 nm  
436 Chroma ET430/24x, BS: LP 455 Leica 11536022, Em: 470/24 nm Chroma ET470/24m), GFP (Ex:  
437 470/40 nm Chroma ET470/40x, BS: LP 498 Leica 11536022, Em: 520/40 nm Chroma ET520/40m),  
438 YFP (Ex: 500/20 nm Chroma ET500/20x, BS: LP 520 Leica 11536022, Em: 535/30 nm Chroma  
439 ET535/30m) and mCherry (Chroma 49017, Ex: 560/40 nm, BS: LP 590 nm, Em: LP 590 nm).  
440 DeltaVision microscope used a DV Quad-mCherry filter set: GFP (Ex: 475/28 nm, BS: 525/80 nm,  
441 Em: 523/36 nm) and mCherry (Ex: 575/25 nm, BS: 605/50, Em: 632/60 nm). Images were processed  
442 using either LAS X (Leica) or SoftWoRx (GE Healthcare). For *S. aureus* microscopy, cells were  
443 induced as described above, grown until  $OD_{600nm} = 0.2$  and analyzed on a Zeiss AxioObserver with an  
444 ORCA $\square$ Flash4.0 V2 Digital CMOS camera (Hamamatsu Photonics) through a 100x PC objective.  
445 HPX 120 Illuminator (Zeiss) was used as a light source for fluorescence microscopy. Images were  
446 processed using ZEN (Zeiss). Signals was deconvolved, when appropriate, using Huygens (SVI)  
447 software.

448

#### 449 **Transmission Electron Microscopy (TEM)**

450 Strains were grown in C+Y medium at either 37°C, or at 30°C for *dnaA<sup>TS</sup>*, until an OD<sub>595nm</sub> = 0.3, with  
451 or without addition of ZnCl<sub>2</sub> (for *ccrZ* complementation or depletion, respectively) and diluted 100  
452 times into 10 mL of fresh C+Y medium. Cells were then grown either at 37°C or at 40°C, for *dnaA*  
453 depletion in the *dnaA<sup>TS</sup>* strain, until OD<sub>595nm</sub> = 0.15. 5 mL of each sample was then fixed with 2.5 %  
454 glutaraldehyde solution (EMS) in phosphate buffer (PB 0.1 M pH = 7.4) (Sigma Aldrich) for 1h at  
455 room temperature, followed by 16 h incubation at 4°C. Cells were then post-fixed by a fresh mixture  
456 of osmium tetroxide 1 % (EMS) with 1.5 % potassium ferrocyanide (Sigma Aldrich) in PB buffer for  
457 2 h at room temperature. Samples were then washed three times with distilled water and spun down in  
458 low melting agarose 2 % (Sigma Aldrich) and solidified in ice. Solid samples were then cut in 1 mm<sup>3</sup>  
459 cubes and dehydrated in acetone solution (Sigma Aldrich) at graded concentrations (30 % for 40 min;  
460 50 % for 40 min; 70 % for 40 min and 100 % for 3 x 1 h). This step was followed by infiltration in  
461 Epon (Sigma Aldrich) at graded concentrations (Epon 1/3 acetone for 2 h; Epon 3/1 acetone for 2 h,  
462 Epon 1/1 for 4 h and Epon 1/1 for 12 h) and finally polymerized for 48 h at 60°C. Ultra-thin sections  
463 of 50 nm were then cut on a Leica Ultracut (Leica Mikrosysteme GmbH) and placed on a copper slot  
464 grid 2 x 1 mm (EMS) coated with a polystyrene film (Sigma Aldrich). Sections were subsequently  
465 post-stained with 4 % uranyl acetate (Sigma Aldrich) for 10 min, rinsed several times with water, then  
466 with Reynolds lead citrate (Sigma Aldrich) for 10 min and rinsed several times with distilled water.  
467 Micrographs were taken using a transmission electron microscope Philips CM100 (Thermo Fisher  
468 Scientific) equipped with a TVIPS TemCam-F416 digital camera (TVIPS) and using an acceleration  
469 voltage of 80 kV. Number of septa and cell length were manually measured on TEM images of cells  
470 in the correct focal plane: 22 wild type cells, 28 CcrZ-depleted cells and 17 CcrZ-complemented cells.

471

### 472 **3D Structured Illumination Microscopy (3D-SIM)**

473 Samples for 3D-SIM were prepared as described previously by spotting 1 µL onto PBS-10 %  
474 acrylamide pads. Acquisition was performed on a DeltaVision OMX SR microscope (GE Healthcare)  
475 equipped with a 60x/1.42 NA objective (Olympus) and 488 nm and 568 nm excitation lasers. 16 Z-  
476 sections of 0.125 µm each were acquired in Structure Illumination mode with 20 ms exposure and 20

477 % laser power. The 240 images obtained were reconstructed with a Wiener constant of 0.01, and the  
478 volume reconstructed using SoftWoRx.

479

#### 480 **Image analysis and cells segmentation**

481 All microscopy images were processed using Fiji (fiji.sc). Cell segmentation based on phase contrast  
482 images was performed either on Oufiti<sup>65</sup>, MicrobeJ<sup>66</sup> or Morphometrics<sup>67</sup> and fluorescent signals where  
483 analyzed using Oufiti (for CcrZ and FtsZ), MicrobeJ<sup>66</sup> (for CcrZ) or iSBatch<sup>68</sup> (for DnaN and *oriC*).

484 Fluorescence heat-maps were generated using BactMAP<sup>69</sup>.

485

#### 486 **Small-scale expression and GFP resin pull-down of FtsZ and CcrZ-GFP**

487 For affinity purification of CcrZ<sub>Sp</sub>-GFP while expressing FtsZ<sub>Sp</sub>, *ccrZ<sub>Sp</sub>* was amplified from D39V  
488 genomic DNA with primers 213/214 and the resulting fragment was assembled using Golden Gate  
489 allelic replacement strategy (BsaI) with plasmid pET-Gate2 ccdB (pSG436), pSG366, pSG367 and  
490 pSG2562, resulting in plasmid pSG2950. *ftsZ* was amplified by PCR 215/216 on D39V genomic  
491 DNA and cloned into plasmid pJet1.2, resulting in plasmid pSG4227. The later was then assembled  
492 with pSG1694 using Golden Gate assembly, leading to plasmid pSG4268. BL21 DE3 Gold competent  
493 cells were co-transformed with plasmids containing one of each *S. pneumoniae* FtsZ and CcrZ-GFP.  
494 Expression was ZYM-5052 autoinduction media<sup>70</sup>. Cells were sonicated in buffer containing 50 mM  
495 Tris pH 7.5, 150 mM potassium acetate, 5 % glycerol, and 5 mM β-mercaptoethanol (lysis buffer).  
496 Supernatant was then mixed with GFP resin which was produced by crosslinking nanobody<sup>71</sup> to NHS-  
497 Activated Sepharose 4 Fast Flow beads (GE Healthcare) according to the manufacturer's instructions.  
498 After 1 hour of batch binding, resin was washed 10 column volume (CV) with lysis buffer. Beads  
499 were then re-suspended in 50 μL of lysis buffer mixed with SDS-PAGE loading dye containing 5 %  
500 w/v β-mercaptoethanol and heat treated at 95 °C for 15 minutes. Supernatant was collected and  
501 labelled heat elution (HE) samples. Whole cell lysate (WC), supernatant after sonication (S), and HE  
502 were loaded on 15 % SDS-PAGE gels and visualized by Coomassie staining.

503

#### 504 **Large-scale purification of CcrZ-CPD for antibody production**

505 In order to express a fusion of *S. pneumoniae* CcrZ with a C-terminal cysteine protease domain  
506 (CPD), *ccrZ* was amplified by PCR from D39V genomic DNA with primers 213/214 and assembled  
507 using Golden Gate allelic replacement strategy (BsaI) with plasmid pET-Gate2 ccdB (pSG436),  
508 pSG366, pSG367 and pSG2559. The resulting pSG2949 plasmid was then transformed into BL21  
509 DE3 Gold cells using ZYM-5052 auto-induction media<sup>70</sup>. Cells were sonicated in buffer containing  
510 300 mM NaCl, 50 mM Tris pH 7.5, 5 mM  $\beta$ -mercaptoethanol, and protease inhibitor cocktail (PIC).  
511 Supernatant was loaded onto a gravity flow column containing HisPur<sup>TM</sup> Cobalt Resin (Thermo  
512 Scientific). Column was washed 5 CV with buffer containing 100 mM NaCl, 20 mM Tris pH 7.5, 5  
513 mM  $\beta$ -mercaptoethanol. Because CcrZ had affinity to the resin even without the CPD, instead of on  
514 column tag cleavage, elution was collected with buffer containing 150 mM Imidazole, 100 mM NaCl,  
515 20 mM Tris pH 7.5, 5 mM  $\beta$ -mercaptoethanol, and tag cleavage was performed for 1 hour at 4 °C by  
516 adding 1 mM inositol hexakisphosphate. The sample was further purified using a HitrapQ column and  
517 Superdex 200 16/600 pg column (GE). The final storage buffer contained 100 mM NaCl, 20 mM Tris  
518 pH 7.5, 1 mM DTT. For antibody production, sample was loaded onto a 15 % SDS PAGE gel. Edge  
519 wells were cut out and stained with Coomassie to determine position of CcrZ on the gel. Gel portions  
520 containing CcrZ was sent for antibody production by Eurogentec.

521

## 522 **Western blot analysis**

523 Cells were grown in C+Y medium until OD<sub>595nm</sub> = 0.2 and harvested by centrifugation at 8000 x g for  
524 2 min at room temperature from 1 mL of culture. Cells were re-suspended into 150  $\mu$ L of Nuclei lysis  
525 buffer (Promega) containing 0.05 % SDS, 0.025% deoxycholate and 1 % Protease Inhibitor Cocktail  
526 (Sigma Aldrich), and incubated at 37°C for 20 min and at 80°C for 5 min in order to lyse them. One  
527 volume of 4X SDS sample buffer (50 mM Tris-HCl pH = 6.8, 2 % SDS, 10 % glycerol, 1 %  $\beta$ -  
528 mercaptoethanol, 12.5 mM EDTA and 0.02 % Bromophenol blue) was then added to three volumes of  
529 cell lysate sample and heated at 95°C for 10 min. Protein samples were separated by SDS-PAGE (4-  
530 20%) and blotted onto polyvinylidene fluoride membranes (Merck Millipore). Membranes were  
531 blocked for 1 h with Tris-buffered saline (TBS) containing 0.1 % Tween 20 (Sigma Aldrich) and 5 %  
532 dry milk and further incubated for 1 h with primary antibodies diluted in TBS, 0.1 % Tween 20, 5 %

533 dry milk. Polyclonal CcrZ-antiserum concentration used was 1:5000 and commercial monoclonal  
534 GFP-IgG (Thermo Fisher Scientific) were used at 1:5000. Membranes were washed four times for 5  
535 min in TBS, 0.1 % Tween 20 and incubated for 1 h with the secondary IgG (HRP-conjugated donkey  
536 anti-rabbit antibodies, Promega) diluted 1:20,000 in TBS, 0.1 % Tween 20 and 5 % dry milk.  
537 Membranes were then washed four times for 5 min in TBS, 0.1 % Tween 20 and revealed with  
538 Immobilon Western HRP substrate (Merck Millipore).

539

#### 540 **ccrZ-GFP purification with anti-GFP nanobodies**

541 *gfp-ccrZ* and *P3-gfp* (negative control) strains were grown in C+Y medium at 37°C until  $OD_{595nm} =$   
542 0.2 and cells were harvested by centrifugation 15 min at 3000 x g at 4°C. Cells were then incubated in  
543 sucrose buffer (0.1 M Tris-HCl pH = 7.5, 2 mM MgCl<sub>2</sub>, 1 M sucrose, 1 % Protease Inhibitor Cocktail  
544 (Sigma Aldrich), 200 µg.mL<sup>-1</sup> RNase A and 10 µg.mL<sup>-1</sup> DNase (Sigma Aldrich)) for 30 min at 30°C,  
545 then incubated in hypotonic buffer (0.1 M Tris-HCl pH = 7.5, 1 mM EDTA, 1 % Triton, 1 % Protease  
546 Inhibitor Cocktail, 200 µg.mL<sup>-1</sup> RNase A and 10 µg.mL<sup>-1</sup> DNase) for 15 min at room temperature and  
547 cell debris were eliminated by centrifugation 30 min at 15,000 x g at 4°C. Cell lysate was then  
548 incubated with equilibrated GFP-Trap resin (Chromotek) at 4°C for 2 h. After several washes with  
549 wash buffer (10 mM Tris-HCl pH = 7.5, 150 mM NaCl, 0.5 mM EDTA, 1 % Protease Inhibitor  
550 Cocktail), beads were resuspended in 20 µL 8 M Urea, 50 mM triethylammonium bicarbonate  
551 (TEAB), pH = 8.0 and reduced with 5 mM DTT for 30 min at 37°C. Cysteines were alkylated by  
552 adding 20 mM iodoacetamide and incubated for 30 min at room temperature in the dark. Samples  
553 were diluted 1:1 with TEAB buffer and digested by adding 0.1 µg of modified Trypsin (Promega) and  
554 incubated overnight at 37°C, followed by a second digestion for 2 h with the same amount of enzyme.  
555 The supernatant was collected, diluted 2 times with 0.1 % formic acid and desalted on strong cation  
556 exchange micro-tips (StageTips, Thermo Fisher scientific) as described<sup>72</sup>. Peptides were eluted with  
557 1.0 M ammonium acetate (100 µL). Dried samples were resuspended in 25 µL 0.1 % formic acid, 2 %  
558 acetonitrile prior being subjected to nano LC-MS/MS.

559

#### 560 **LC-MS/MS analysis**

561 Tryptic peptide mixtures (5  $\mu$ L) were injected on a Dionex RSLC 3000 nanoHPLC system (Dionex,  
562 Sunnyvale, CA, USA) interfaced via a nanospray source to a high resolution QExactive Plus mass  
563 spectrometer (Thermo Fisher Scientific). Peptides were separated on an Easy Spray C18 PepMap  
564 nanocolumn (25 or 50 cm x 75  $\mu$ m ID, 2  $\mu$ m, 100  $\text{\AA}$ , Dionex) using a 35 min gradient from 4 to 76 %  
565 acetonitrile in 0.1 % formic acid for peptide separation (total time: 65 min). Full MS survey scans  
566 were performed at 70,000 resolution. In data-dependent acquisition controlled by Xcalibur software  
567 (Thermo Fisher), the 10 most intense multiply charged precursor ions detected in the full MS survey  
568 scan were selected for higher energy collision-induced dissociation (HCD, normalized collision  
569 energy NCE = 27 %) and analysis in the orbitrap at 17,500 resolution. The window for precursor  
570 isolation was of 1.6 m/z units around the precursor and selected fragments were excluded for 60 sec  
571 from further analysis.

572 MS data were analyzed using Mascot 2.5 (Matrix Science, London, UK) set up to search the  
573 UniProt ([www.uniprot.org](http://www.uniprot.org)) protein sequence database restricted to *S. pneumoniae* D39 / NCTC 7466  
574 taxonomy (339 SWISSPROT sequences + 1586 TrEMBL sequences). Trypsin (cleavage at K,R) was  
575 used as the enzyme definition, allowing 2 missed cleavages. Mascot was searched with a parent ion  
576 tolerance of 10 ppm and a fragment ion mass tolerance of 0.02 Da (QExactive Plus). Iodoacetamide  
577 derivative of cysteine was specified in Mascot as a fixed modification. N-terminal acetylation of  
578 protein, oxidation of methionine and phosphorylation of Ser, Thr, Tyr and His were specified as  
579 variable modifications. Scaffold software (version 4.4, Proteome Software Inc., Portland, OR) was  
580 used to validate MS/MS based peptide and protein identifications, and to perform dataset alignment.  
581 Peptide identifications were accepted if they could be established at greater than 90.0 % probability as  
582 specified by the Peptide Prophet algorithm<sup>73</sup> with Scaffold delta-mass correction. Protein  
583 identifications were accepted if they could be established at greater than 95.0 % probability and  
584 contained at least 2 identified peptides. Protein probabilities were assigned by the Protein Prophet  
585 algorithm<sup>74</sup>. Proteins that contained similar peptides and could not be differentiated based on MS/MS  
586 analysis alone were grouped to satisfy the principles of parsimony. Proteins sharing significant  
587 peptide evidence were grouped into clusters.

588

589 **Split luciferase assay**

590 *S. pneumoniae* cells were grown in C+Y medium at 37°C until  $OD_{595nm} = 0.2$  and washed once with  
591 fresh C+Y medium. 1 % NanoGlo Live Cell substrate (Promega) was then added, and luminescence  
592 was measured 20 times at 37°C every 30 sec in plate reader (TECAN Infinite F200 Pro).  
593 Measurements were performed in triplicate and the average values were plotted, with the SEM  
594 (Standard Error of the Mean) represented by the dot size.

595

596 **Bacterial two-hybrid assay**

597 The bacterial two-hybrid assay was based on the method from Karimova *et al.*<sup>43</sup> with the following  
598 modifications. *dnaA*, *ccrZ* and *ftsZ* genes from *S. pneumoniae* D39V were cloned both into the low  
599 copy-number vector pUT18 and into the high copy-number vector pST25<sup>75</sup> using the enzymes BamHI  
600 and KpnI. *Escherichia coli* strain HM1784 (BTH101  $\Delta rnh::kan$ ) was transformed using each  
601 combination of plasmids. Chemically competent cells were incubated on ice for 60 min, heat shocking  
602 at 42°C for 90 sec and then inoculated at 37°C in 3 mL of LB media supplemented with ampicillin (100  
603 µg/mL) and spectinomycin (50 µg/mL) with mild agitation for 16 hours. The  $A_{600nm}$  was adjusted to  
604 0.5, cultures were diluted 1:1000 and a 5 µL aliquot was spotted on a nutrient agar plate containing  
605 antibiotics (as above) containing 0.006 % X-gal. Plates were incubated at 30°C for 48 hours and the  
606 images were captured using a digital camera.

607

608 **Co-immunoprecipitation of CcrZ and FtsZ-GFP with anti-GFP nanobodies**

609 *S. pneumoniae* cells were grown in C+Y medium at 37°C until  $OD_{595nm} = 0.2$  and harvested by  
610 centrifugation 15 min at 3,000 x g at 4°C. Cells were lysed using GFP-Trap\_A Lysis buffer  
611 (Chromotek), 0.25 % Deoxycolate, 1 % Protease Inhibitor Cocktail incubated at room temperature for  
612 10 min followed by incubation at 4°C for 20 min. Cell lysate was incubated with equilibrated GFP-  
613 Trap resin (Chromotek) at 4°C for 2 h. The resin was then washed 3 times in GFP-Trap\_A Wash  
614 buffer (Chromotek) and GFP-proteins were eluted using SDS sample buffer at 95°C for 10 min and  
615 analyzed by immunoblotting.



616

### 617 **Genome resequencing of *ccrZ* suppressors by NGS**

618 Strains *hlpA-mKate2 ΔccrZ*, *ccrZ<sup>supp1</sup>*, *ccrZ<sup>supp2</sup>* and *ccrZ<sup>supp3</sup>* were grown in C+Y medium at 37°C  
619 until OD<sub>595nm</sub> = 0.3 and cells were harvested by centrifugation 1 min at 10,000 x g. Pellet was then re-  
620 suspended into Nuclei lysis buffer (Promega) containing 0.05 % SDS, 0.025% deoxycholate and 200  
621 μg.mL<sup>-1</sup> RNase A at 37°C for 20 min to lyse the cells and Protein Precipitation Solution (Promega)  
622 was added. DNA was then precipitated using isopropanol. The extracted genomes were then analyzed  
623 by Illumina sequencing by GATC Biotech (Eurofins Genomics). Mutations were mapped onto D39V  
624 genome using breseq pipeline<sup>76</sup>. Genomes sequences are available at SRA (project PRJNA564501).

625

### 626 ***oriC/ter* ratios determination by RT-qPCR**

627 Determination of *S. pneumoniae oriC/ter* ratios was performed as followed. Cells were pre-grown  
628 until OD<sub>600nm</sub> = 0.4 in C+Y medium at 37°C, with or without inducer (ZnCl<sub>2</sub> or IPTG) for  
629 complementation and depletion conditions, respectively. Cells were then diluted 100 times in fresh  
630 C+Y medium supplemented when appropriate with inducer and harvested for genomic DNA isolation  
631 when they reached OD<sub>600nm</sub> = 0.1 (exponential phase). For normalization (*oriC/ter* ratio of 1), *dnaA*  
632 thermosensitive strain was grown for 2h at non-permissive temperature (40°C) in C+Y medium and  
633 harvested for chromosomal DNA isolation. As a negative (overinitiating) control, wild type *S.*  
634 *pneumoniae* was incubated 2h with 0.15 μg.mL<sup>-1</sup> HPUra (DNA replication inhibitor) at 37°C prior to  
635 harvesting. Primers pairs OT1/OT2 and OT3/OT4 were used to amplify the *oriC* and *ter* regions  
636 respectively. Amplification by Real-Time qPCR was performed using SYBR Select Master Mix  
637 (Applied Biosystems) on a StepOne Plus Real-Time PCR System (Applied Biosystems), in triplicate.  
638 For *S. aureus oriC/ter* ratio determination, overnight cultures were diluted 100-fold and grown until  
639 OD<sub>600nm</sub> = 0.4. These cultures were then re-diluted 200-fold in medium with 500 μM IPTG and grown  
640 until OD<sub>600nm</sub> = 0.2. As reference samples with assumed *oriC/ter* ratio of 1, wild type *S. aureus*  
641 SH1000 cells at OD<sub>600nm</sub> = 0.15 were supplemented with 50 μg.mL<sup>-1</sup> rifampicin (inhibiting replication  
642 initiation) and incubated for 2 hours for replication run-out. Cells were then harvested and lysed  
643 enzymatically by addition of 0.2 mg.mL<sup>-1</sup> lysostaphin and 10 mg.mL<sup>-1</sup> lysozyme, and genomic DNA

644 was isolated using the Wizard Genomic DNA Purification Kit (Promega). qPCR reactions of 10  $\mu$ L  
645 were set up with 5  $\mu$ L PowerUp™ SYBR™ Green Master Mix (Applied Biosystems), 500 nM of  
646 each primer OT5/OT and OT7/OT8 and 20 ng of DNA. In both cases, amplification efficiencies of the  
647 primers and *oriC/ter* ratios were determined as described previously<sup>46</sup>. Data were plotted as whiskers  
648 plot where whiskers represent the 10<sup>th</sup> and 90<sup>th</sup> percentile of data from Monte Carlo simulations, \* P  
649 value < 0.05, significantly up. For *B. subtilis oriC/ter* ratios determination, cultures were grown to  
650 mid-exponential phase in LB medium and diluted back to OD<sub>600nm</sub> = 0.05 and grown to mid-  
651 exponential phase (OD<sub>600nm</sub> = 0.2 - 0.4) at 37°C. Cells were harvested in ice-cold methanol (1:1 ratio)  
652 and pelleted. Genomic DNA was isolated using Qiagen DNeasy kit with 40  $\mu$ g.mL<sup>-1</sup> lysozyme. The  
653 copy number of the origin (*oriC*) and terminus (*ter*) were quantified by qPCR to generate the *oriC/ter*  
654 ratio. qPCR was done using SSoAdvanced SYBR master mix and CFX96 Touch Real-Time PCR  
655 system (Bio-Rad). Primers used to quantify the origin region were OT9/OT10. Primers used to  
656 quantify the terminus region were OT11/OT12. Origin-to-terminus ratios were determined by  
657 dividing the number of copies (as indicated by the Cp values measured through qPCRs) of the origin  
658 by the number of copies quantified at the terminus. Ratios were normalized to the origin-to-terminus  
659 ratio of a temperature sensitive mutant, *dnaB134* (KPL69), that was grown to have synchronized  
660 replication initiation, resulting in 1:1 ratio of the *oriC/ter*. Data were plotted as whiskers plot. \*P  
661 value < 0.05 (t-test), significantly up.

662

### 663 **Genetic interactions determination by CRISPRi-seq**

664 Protocol for CRISPRi library construction, sequencing and analysis was performed as described  
665 before<sup>49</sup>. Briefly, 1,499 plasmids containing a different sgRNA were transformed into strain *P<sub>ter</sub>-*  
666 *dCas9*, *P<sub>lac-ccrZ</sub>*,  $\Delta$ *ccrZ* in presence of 1 mM IPTG to ensure the expression of wild type *ccrZ*,  
667 resulting in a pooled library containing the inducible CRISPRi system under control of an  
668 anhydrotetracycline (aTc) -inducible promoter and combined with a depletion of *ccrZ* under control of  
669 an IPTG-inducible promoter. Colonies were harvested and stored at -80°C. To ensure sufficient  
670 induction of the library, cells were grown for 8 generations in triplicates. The pooled libraries were  
671 diluted 1:100 from stock in 10 mL of CY medium supplemented or not with aTc 50 ng.mL<sup>-1</sup> and 1

672 mM IPTG and grown at 37°C. At  $OD_{600nm} = 0.4$ , cells were harvested and their gDNA isolated and  
673 prepared for MiniSeq (Illumina) sequencing with a custom sequencing protocol  
674 ([www.veeninglab.com/crispri-seq](http://www.veeninglab.com/crispri-seq)). sgRNA counts were retrieved and analyzed using DESeq2  
675 package in R to evaluate the fitness cost of each sgRNA as previously described<sup>49</sup>. The effect of  
676 interaction between aTc treatments, across *ccrZ* complementation and depletion was compared with a  
677  $\log_2FC$  of 1 and an alpha of 0.05.

678

### 679 **Quantifications and statistical analysis**

680 Data analysis was performed using R and Prism (Graphpad). When comparing wild type phenotypes  
681 with *ccrZ* depletion/complementation, a Wilcoxon rank sum test with Bonferroni adjustment was used  
682 as we did not assume a normal distribution, since some mutant cells can behave like wild type  
683 because of the variable time of depletion or possible leakiness of  $P_{lac}$  or  $P_{Zn}$ . When using whiskers  
684 plot, the lower and upper whiskers represent, respectively, the minimum and maximum values of the  
685 data; the median is represented as a solid line and the lower and upper quartiles respectively represent  
686 the 25<sup>th</sup> and 75<sup>th</sup> percentiles. When plotting the *oriC/ter* ratios in Fig. 4, the outliers are also depicted  
687 by gray dots.

688 Data shown are represented as mean of at least three replicates  $\pm$  SEM if data came from one  
689 experiment with replicated measurement, and  $\pm$  SD if data came from separate experiments.

690

### 691 **Data availability**

692 The data that support the findings of this study are available from the corresponding author upon  
693 request. Genomes sequences data are available at NCBI Sequence Read Archive (SRA) under the  
694 following accession number [PRJNA564501](https://www.ncbi.nlm.nih.gov/sra/PRJNA564501).

695

696 **References**

- 697 1. Harashima, H., Dissmeyer, N. & Schnittger, A. Cell cycle control across the eukaryotic  
698 kingdom. *Trends Cell Biol.* **23**, 345–356 (2013).
- 699 2. Boye, E. & Nordström, K. Coupling the cell cycle to cell growth. *EMBO Rep.* **4**, 757–60  
700 (2003).
- 701 3. Reyes-Lamothe, R. & Sherratt, D. J. The bacterial cell cycle, chromosome inheritance and cell  
702 growth. *Nat. Rev. Microbiol.* **1** (2019) doi:10.1038/s41579-019-0212-7.
- 703 4. Kjeldgaard, N. O., MaalOe, O. & Schaechter, M. The Transition Between Different  
704 Physiological States During Balanced Growth of *Salmonella typhimurium*. *J. Gen. Microbiol.*  
705 **19**, 607–616 (1958).
- 706 5. Schaechter, M., MaalOe, O. & Kjeldgaard, N. O. Dependency on Medium and Temperature of  
707 Cell Size and Chemical Composition during Balanced Growth of *Salmonella typhimurium*. *J.*  
708 *Gen. Microbiol.* **19**, 592–606 (1958).
- 709 6. Donachie, W. D. Relationship between cell size and time of initiation of DNA replication.  
710 *Nature* **219**, 1077–9 (1968).
- 711 7. Cooper, S. & Helmstetter, C. E. Chromosome replication and the division cycle of *Escherichia*  
712 *coli* Br. *J. Mol. Biol.* **31**, 519–540 (1968).
- 713 8. Campos, M. *et al.* A Constant Size Extension Drives Bacterial Cell Size Homeostasis. *Cell*  
714 **159**, 1433–1446 (2014).
- 715 9. Taheri-Araghi, S. *et al.* Cell-size control and homeostasis in bacteria. *Curr. Biol.* **25**, 385–391  
716 (2015).
- 717 10. Wold, S., Skarstad, K., Steen, H. B., Stokke, T. & Boye, E. The initiation mass for DNA  
718 replication in *Escherichia coli* K-12 is dependent on growth rate. *EMBO J.* **13**, 2097–102  
719 (1994).
- 720 11. Si, F. *et al.* Mechanistic Origin of Cell-Size Control and Homeostasis in Bacteria. *Curr. Biol.*  
721 **29**, 1760-1770.e7 (2019).
- 722 12. Wallden, M., Fange, D., Lundius, E. G., Baltekin, Ö. & Elf, J. The Synchronization of

- 723            Replication and Division Cycles in Individual *E. coli* Cells. *Cell* **166**, 729–739 (2016).
- 724    13.    Kleckner, N. E., Chatzi, K., White, M. A., Fisher, J. K. & Stouf, M. Coordination of Growth,  
725            Chromosome Replication/Segregation, and Cell Division in *E. coli*. *Front. Microbiol.* **9**, 1469  
726            (2018).
- 727    14.    Kleckner, N. *et al.* The bacterial nucleoid: nature, dynamics and sister segregation. *Curr. Opin.*  
728            *Microbiol.* **22**, 127–37 (2014).
- 729    15.    Hajduk, I. V., Rodrigues, C. D. A. & Harry, E. J. Connecting the dots of the bacterial cell  
730            cycle: Coordinating chromosome replication and segregation with cell division. *Semin. Cell*  
731            *Dev. Biol.* **53**, 2–9 (2016).
- 732    16.    Espéli, O. *et al.* A MatP-divisome interaction coordinates chromosome segregation with cell  
733            division in *E. coli*. *EMBO J.* **31**, 3198–211 (2012).
- 734    17.    Zheng, H. *et al.* Interrogating the *Escherichia coli* cell cycle by cell dimension perturbations.  
735            *Proc. Natl. Acad. Sci. U. S. A.* **113**, 15000–15005 (2016).
- 736    18.    Huls, P. G., Vischer, N. O. E. & Woldringh, C. L. Different Amounts of DNA in Newborn  
737            Cells of *Escherichia coli* Preclude a Role for the Chromosome in Size Control According to  
738            the “Adder” Model. *Front. Microbiol.* **9**, 664 (2018).
- 739    19.    Katayama, T. Initiation of DNA Replication at the Chromosomal Origin of *E. coli*, *oriC*. in  
740            79–98 (Springer, Singapore, 2017). doi:10.1007/978-981-10-6955-0\_4.
- 741    20.    Katayama, T., Kasho, K. & Kawakami, H. The DnaA Cycle in *Escherichia coli*: Activation,  
742            Function and Inactivation of the Initiator Protein. *Front. Microbiol.* **8**, 2496 (2017).
- 743    21.    Løbner-Olesen, A., Skarstad, K., Hansen, F. G., von Meyenburg, K. & Boye, E. The DnaA  
744            protein determines the initiation mass of *Escherichia coli* K-12. *Cell* **57**, 881–889 (1989).
- 745    22.    Pierucci, O., Rickert, M. & Helmstetter, C. E. DnaA protein overproduction abolishes cell  
746            cycle specificity of DNA replication from *oriC* in *Escherichia coli*. *J. Bacteriol.* **171**, 3760–6  
747            (1989).
- 748    23.    Flåtten, I., Fossum-Raunehaug, S., Taipale, R., Martinsen, S. & Skarstad, K. The DnaA  
749            Protein Is Not the Limiting Factor for Initiation of Replication in *Escherichia coli*. *PLOS*  
750            *Genet.* **11**, e1005276 (2015).

- 751 24. Hill, N. S., Kadoya, R., Chattoraj, D. K. & Levin, P. A. Cell Size and the Initiation of DNA  
752 Replication in Bacteria. *PLoS Genet.* **8**, e1002549 (2012).
- 753 25. Murray, H. & Koh, A. Multiple Regulatory Systems Coordinate DNA Replication with Cell  
754 Growth in *Bacillus subtilis*. *PLoS Genet.* **10**, e1004731 (2014).
- 755 26. Bisicchia, P., Arumugam, S., Schwille, P. & Sherratt, D. MinC, MinD, and MinE drive  
756 counter-oscillation of early-cell-division proteins prior to *Escherichia coli* septum formation.  
757 *MBio* **4**, e00856-13 (2013).
- 758 27. Marston, A. L., Thomaidis, H. B., Edwards, D. H., Sharpe, M. E. & Errington, J. Polar  
759 localization of the MinD protein of *Bacillus subtilis* and its role in selection of the mid-cell  
760 division site. *Genes Dev.* **12**, 3419–30 (1998).
- 761 28. Wu, L. J. & Errington, J. Nucleoid occlusion and bacterial cell division. *Nat. Rev. Microbiol.*  
762 **10**, 8–12 (2012).
- 763 29. Pinho, M. G., Kjos, M. & Veening, J.-W. How to get (a)round: mechanisms controlling  
764 growth and division of coccoid bacteria. *Nat. Rev. Microbiol.* **11**, 601–614 (2013).
- 765 30. Land, A. D. *et al.* Requirement of essential Pbp2x and GpsB for septal ring closure in  
766 *Streptococcus pneumoniae* D39. *Mol. Microbiol.* **90**, 939–955 (2013).
- 767 31. Mercy, C. *et al.* RocS drives chromosome segregation and nucleoid protection in  
768 *Streptococcus pneumoniae*. *Nat. Microbiol.* **4**, 1661–1670 (2019).
- 769 32. Fleurie, A. *et al.* MapZ marks the division sites and positions FtsZ rings in *Streptococcus*  
770 *pneumoniae*. *Nature* **516**, 259–262 (2014).
- 771 33. Holečková, N. *et al.* LocZ is a new cell division protein involved in proper septum placement  
772 in *Streptococcus pneumoniae*. *MBio* **6**, e01700-14 (2014).
- 773 34. Perez, A. J. *et al.* Movement dynamics of divisome proteins and PBP2x:FtsW in cells of  
774 *Streptococcus pneumoniae*. *Proc. Natl. Acad. Sci.* **116**, 3211–3220 (2019).
- 775 35. van Raaphorst, R., Kjos, M. & Veening, J.-W. Chromosome segregation drives division site  
776 selection in *Streptococcus pneumoniae*. *Proc. Natl. Acad. Sci. U. S. A.* **114**, E5959–E5968  
777 (2017).
- 778 36. Liu, X. *et al.* High-throughput CRISPRi phenotyping identifies new essential genes

- 779           inStreptococcus pneumoniae. *Mol. Syst. Biol.* **13**, 931 (2017).
- 780   37.   Nourikyan, J. *et al.* Autophosphorylation of the Bacterial Tyrosine-Kinase CpsD Connects  
781   Capsule Synthesis with the Cell Cycle in Streptococcus pneumoniae. *PLOS Genet.* **11**,  
782   e1005518 (2015).
- 783   38.   Du, S. & Lutkenhaus, J. Assembly and activation of the *Escherichia coli* divisome. *Mol.*  
784   *Microbiol.* **105**, 177–187 (2017).
- 785   39.   Beilharz, K., van Raaphorst, R., Kjos, M. & Veening, J. W. Red fluorescent proteins for gene  
786   expression and protein localization studies in Streptococcus pneumoniae and efficient  
787   transformation with DNA assembled via the gibson assembly method. *Appl. Environ.*  
788   *Microbiol.* **81**, 7244–7252 (2015).
- 789   40.   Krogh, A., Larsson, B., von Heijne, G. & Sonnhammer, E. L. . Predicting transmembrane  
790   protein topology with a hidden markov model: application to complete genomes. *J. Mol. Biol.*  
791   **305**, 567–580 (2001).
- 792   41.   Oliveira Paiva, A. M. *et al.* The Bacterial Chromatin Protein HupA Can Remodel DNA and  
793   Associates with the Nucleoid in Clostridium difficile. *J. Mol. Biol.* **431**, 653–672 (2019).
- 794   42.   Bodle, C. R., Hayes, M. P., O’Brien, J. B. & Roman, D. L. Development of a bimolecular  
795   luminescence complementation assay for RGS: G protein interactions in cells. *Anal. Biochem.*  
796   **522**, 10–17 (2017).
- 797   43.   Karimova, G., Pidoux, J., Ullmann, A. & Ladant, D. A bacterial two-hybrid system based on a  
798   reconstituted signal transduction pathway. *Proc. Natl. Acad. Sci. U. S. A.* **95**, 5752–6 (1998).
- 799   44.   Kjos, M. *et al.* Bright fluorescent Streptococcus pneumoniae for live-cell imaging of host-  
800   pathogen interactions. *J. Bacteriol.* **197**, 807–18 (2015).
- 801   45.   Felicori, L. *et al.* Tetramerization and interdomain flexibility of the replication initiation  
802   controller YabA enables simultaneous binding to multiple partners. *Nucleic Acids Res.* **44**,  
803   449–463 (2016).
- 804   46.   Slager, J., Kjos, M., Attaiech, L. & Veening, J.-W. Antibiotic-Induced Replication Stress  
805   Triggers Bacterial Competence by Increasing Gene Dosage near the Origin. *Cell* **157**, 395–406  
806   (2014).

- 807 47. Duderstadt, K. E., Chuang, K. & Berger, J. M. DNA stretching by bacterial initiators promotes  
808 replication origin opening. *Nature* **478**, 209–213 (2011).
- 809 48. Scholefield, G., Errington, J. & Murray, H. Soj/ParA stalls DNA replication by inhibiting helix  
810 formation of the initiator protein DnaA. *EMBO J.* **31**, 1542–55 (2012).
- 811 49. Liu, X. *et al.* Exploration of Bacterial Bottlenecks and *Streptococcus pneumoniae*  
812 Pathogenesis by CRISPRi-Seq. *Cell Host Microbe* **29**, 107-120.e6 (2021).
- 813 50. Mercy, C. *et al.* RocS drives chromosome segregation and nucleoid protection in  
814 *Streptococcus pneumoniae*. *Nat. Microbiol.* **1** (2019) doi:10.1038/s41564-019-0472-z.
- 815 51. Bigot, S., Sivanathan, V., Possoz, C., Barre, F.-X. & Cornet, F. FtsK, a literate chromosome  
816 segregation machine. *Mol. Microbiol.* **64**, 1434–1441 (2007).
- 817 52. Soding, J., Biegert, A. & Lupas, A. N. The HHpred interactive server for protein homology  
818 detection and structure prediction. *Nucleic Acids Res.* **33**, W244–W248 (2005).
- 819 53. Wang, L., Jiang, Y.-L., Zhang, J.-R., Zhou, C.-Z. & Chen, Y. Structural and Enzymatic  
820 Characterization of the Choline Kinase LicA from *Streptococcus pneumoniae*. *PLoS One* **10**,  
821 e0120467 (2015).
- 822 54. BRENNER, S. Phosphotransferase sequence homology. *Nature* **329**, 21–21 (1987).
- 823 55. Yu, X. C. & Margolin, W. FtsZ ring clusters in min and partition mutants: Role of both the  
824 Min system and the nucleoid in regulating FtsZ ring localization. *Mol. Microbiol.* **32**, 315–326  
825 (1999).
- 826 56. Harry, E. J., Rodwell, J. & Wake, R. G. Co-ordinating DNA replication with cell division in  
827 bacteria: a link between the early stages of a round of replication and mid-cell Z ring  
828 assembly. *Mol. Microbiol.* **33**, 33–40 (1999).
- 829 57. Pang, T., Wang, X., Lim, H. C., Bernhardt, T. G. & Rudner, D. Z. The nucleoid occlusion  
830 factor Noc controls DNA replication initiation in *Staphylococcus aureus*. *PLoS Genet.* **13**,  
831 e1006908 (2017).
- 832 58. Slager, J., Aprianto, R. & Veening, J.-W. Deep genome annotation of the opportunistic human  
833 pathogen *Streptococcus pneumoniae* D39. *Nucleic Acids Res.* **46**, 9971–9989 (2018).
- 834 59. Domenech, A., Slager, J. & Veening, J.-W. Antibiotic-Induced Cell Chaining Triggers



- 835 Pneumococcal Competence by Reshaping Quorum Sensing to Autocrine-Like Signaling. *Cell*  
836 *Rep.* **25**, 2390-2400.e3 (2018).
- 837 60. Monk, I. R., Tree, J. J., Howden, B. P., Stinear, T. P. & Foster, T. J. Complete Bypass of  
838 Restriction Systems for Major *Staphylococcus aureus* Lineages. *MBio* **6**, e00308-15 (2015).
- 839 61. Löfblom, J., Kronqvist, N., Uhlén, M., Ståhl, S. & Wernérus, H. Optimization of  
840 electroporation-mediated transformation: *Staphylococcus carnosus* as model organism. *J.*  
841 *Appl. Microbiol.* **102**, 736–747 (2007).
- 842 62. Jaacks, K. J., Healy, J., Losick, R. & Grossman, A. D. Identification and characterization of  
843 genes controlled by the sporulation-regulatory gene *spo0H* in *Bacillus subtilis*. *J. Bacteriol.*  
844 **171**, 4121–4129 (1989).
- 845 63. Perego, M., Spiegelman, G. B. & Hoch, J. A. Structure of the gene for the transition state  
846 regulator, *abrB*: regulator synthesis is controlled by the *spo0A* sporulation gene in *Bacillus*  
847 *subtilis*. *Mol. Microbiol.* **2**, 689–699 (1988).
- 848 64. de Jong, I. G., Beilharz, K., Kuipers, O. P. & Veening, J. W. Live cell imaging of *Bacillus*  
849 *subtilis* and *Streptococcus pneumoniae* using automated time-lapse microscopy. *Journal of*  
850 *Visualized Experiments* 3145 (2011) doi:10.3791/3145.
- 851 65. Paintdakhi, A. *et al.* Oufiti: an integrated software package for high-accuracy, high-throughput  
852 quantitative microscopy analysis. *Mol. Microbiol.* **99**, 767–777 (2016).
- 853 66. Ducret, A., Quardokus, E. M. & Brun, Y. V. MicrobeJ, a tool for high throughput bacterial cell  
854 detection and quantitative analysis. *Nat. Microbiol.* **1**, 16077 (2016).
- 855 67. Ursell, T. *et al.* Rapid, precise quantification of bacterial cellular dimensions across a  
856 genomic-scale knockout library. *BMC Biol.* **15**, 17 (2017).
- 857 68. Caldas, V. E. A., Punter, C. M., Ghodke, H., Robinson, A. & van Oijen, A. M. iSBatch: a  
858 batch-processing platform for data analysis and exploration of live-cell single-molecule  
859 microscopy images and other hierarchical datasets. *Mol. Biosyst.* **11**, 2699–2708 (2015).
- 860 69. van Raaphorst, R., Kjos, M. & Veening, J. W. BactMAP: An R package for integrating,  
861 analyzing and visualizing bacterial microscopy data. *Mol. Microbiol.* **113**, 297–308 (2020).
- 862 70. Studier, F. W. Protein production by auto-induction in high density shaking cultures. *Protein*

- 863            *Expr. Purif.* **41**, 207–34 (2005).
- 864    71.    Kubala, M. H., Kovtun, O., Alexandrov, K. & Collins, B. M. Structural and thermodynamic  
865            analysis of the GFP:GFP-nanobody complex. *Protein Sci.* **19**, 2389–401 (2010).
- 866    72.    Kulak, N. A., Pichler, G., Paron, I., Nagaraj, N. & Mann, M. Minimal, encapsulated  
867            proteomic-sample processing applied to copy-number estimation in eukaryotic cells. *Nat.*  
868            *Methods* **11**, 319–324 (2014).
- 869    73.    Keller, A., Nesvizhskii, A. I., Kolker, E. & Aebersold, R. Empirical statistical model to  
870            estimate the accuracy of peptide identifications made by MS/MS and database search. *Anal.*  
871            *Chem.* **74**, 5383–5392 (2002).
- 872    74.    Nesvizhskii, A. I., Keller, A., Kolker, E. & Aebersold, R. A statistical model for identifying  
873            proteins by tandem mass spectrometry. *Anal. Chem.* **75**, 4646–4658 (2003).
- 874    75.    Ouellette, S. P. *et al.* Analysis of MreB interactors in Chlamydia reveals a RodZ homolog but  
875            fails to detect an interaction with MraY. *Front. Microbiol.* **5**, 279 (2014).
- 876    76.    Deatherage, D. E. & Barrick, J. E. Identification of mutations in laboratory-evolved microbes  
877            from next-generation sequencing data using breseq. *Methods Mol. Biol.* **1151**, 165–88 (2014).
- 878

## 879 **Acknowledgements**

880 We appreciate the assistance from the Electron Microscopy Facility (EMF) and the Protein Analysis  
881 Facility (PAF) at the University of Lausanne (UNIL) and thank them for their support. We thank  
882 Wiep Klaas Smits (LUMC) for the Split-luc sequences and Tanneke den Blaauwen (UVA) for the  
883 mTQ<sup>ox</sup> sequence prior to publication, Arnau Domenech (UNIL) for construction of strain *hlpA-LgBit*  
884 *hlpA-SmBit* and Zhian Salehian (NMBU) for help with cloning. Work in the Kjos lab is supported by  
885 a FRIMEDBIO grant (project number 250976) and a JPIAMR grant (project number 296906) from  
886 the Research Council of Norway. Work in the Murray lab was supported by a Wellcome Trust Senior  
887 Research Fellowship (204985/Z/16/Z) and a grant from the Biotechnology and Biological Sciences  
888 Research Council (BB/P018432/1). Work in the Grossman lab was supported, in part, by the National  
889 Institute of General Medical Sciences of the National Institutes of Health under award number R37  
890 GM041934 and R35 GM122538. Work in the Veening lab is supported by the Swiss National Science  
891 Foundation (SNSF) (project grant 31003A\_172861), a JPIAMR grant (40AR40\_185533) from SNSF,  
892 a Novartis Foundation grant (#17B064) and ERC consolidator grant 771534-PneumoCaTChER.

893

## 894 **Author contributions**

895 C.G. and J.W.V. wrote the paper with input from all authors. C.G., S.S., M.E.A., Y.M.S., X.L.,  
896 G.A.S., S.P., R.R., J.D. and M.K. performed the experiments. C.G., S.S., M.E.A., M.K., H.M., S.G.,  
897 A.D.G. and J.W.V. designed, analyzed and interpreted the data.

898

## 899 **Competing interests**

900 The authors declare no competing interests.

901

902

903 **Figure legends**

904 **Fig. 1: Depletion of CcrZ leads to anucleate cells and division defects**

905 **a**, Growth curve of cells with *ccrZ* targeted by CRISPRi (*ccrZ*<sup>sgRNA</sup> + IPTG) indicates a clear growth  
906 defect when *ccrZ* is silenced. **b**, *ccrZ* silencing leads to appearance of anucleate cells, as visualized by  
907 DAPI staining. **c**, *ccrZ* depletion by ectopic expression via the IPTG-inducible Plac promoter also  
908 leads to cells lacking a nucleoid, as observed by DAPI staining. **d**, Distribution of cell area of *ccrZ*-  
909 depleted cells, *ccrZ* depletion leads to a slight decrease in cell length and cell area ( $P$  value =  $2.2 \times 10^{-16}$ ,  
910 Wilcoxon rank sum test). **e**, When a deletion of *ccrZ* is complemented (left panel), FtsZ-  
911 mTurquoise2 shows a clear mid-cell localization, while it appears as a blurry signal in several cells  
912 upon *ccrZ* depletion (right panel). **f**, Transmission electron microscopy (TEM) indicates that cells  
913 depleted for *ccrZ* form multiple, often incomplete, septa. **g**, Distribution of number of septa per cell  
914 length as determined by TEM for 22 wild type cells, 28 CcrZ-depleted cells and 17 CcrZ-  
915 complemented cells. Each dot represents a measurement. ( $P$  value =  $1 \times 10^{-6}$  for wild type vs *ccrZ*-  
916 depleted cells and  $P$  value = 0.0013 for *ccrZ*-complemented vs *ccrZ*-depleted cells, Wilcoxon rank  
917 sum test with Bonferroni adjustment).

918

919 **Fig. 2: CcrZ co-localizes with FtsZ at new division sites**

920 **a**, CcrZ localizes at mid-cell in live wild type *S. pneumoniae* cells as observed by epifluorescence  
921 microscopy of GFP-CcrZ and CcrZ-mKate2. **b**, 3D-SIM of GFP-CcrZ and reconstructed volume  
922 projection (right) indicate that CcrZ forms a patchy ring at mid-cell. **c**, GFP-CcrZ and FtsZ-mCherry  
923 co-localize in wild type cells. **d**, Localization signal of GFP-CcrZ and FtsZ-mCherry in 699 cells of a  
924 double labelled *gfp-ccrZ ftsZ-mCherry* strain, ordered by cell length and represented by a heatmap. **e**,  
925 GFP-CcrZ and FtsZ-mCherry co-localize during the entire cell cycle, as visualized when signal  
926 localization over cell length is grouped in three quantiles. **f**, 3D-SIM co-localization of GFP-CcrZ and  
927 FtsZ-mCherry shows a clear co-localizing ring with identical patchy pattern. Note that for clarity, we  
928 did not correct for chromatic shift in the overlay.

929

930 **Fig. 3: CcrZ directly interacts with FtsZ**

931 **a**, Split-luciferase assay using several combinations with CcrZ-LgBit reveals that CcrZ and FtsZ are  
932 in very close proximity, as indicated by a high luminescence signal. FtsA, EzrA and ZapA, all three  
933 interacting directly with FtsZ, also gave a slight signal. *hlpA-LgBit hlpA-SmBit* (HlpA-HlpA), here  
934 diluted 100 times, is used as positive control. Each dot represents the average of 15 measurements of a  
935 technical replicate, with the size of the dot representing the SEM. **b**, FtsZ-CcrZ interaction  
936 confirmation by bacterial two-hybrid assay. T25 is the empty vector pST25 and T25-FtsZ corresponds  
937 to vector pST25-FtsZ used in combination with pUT18-CcrZ (CcrZ-T18) and pUT18-FtsZ (FtsZ-  
938 T18). **c**, Affinity purification of FtsZ-GFP from *S. pneumoniae* cells (2<sup>nd</sup> lane) also pulls down  
939 untagged CcrZ (4<sup>th</sup> lane). Purification of GFP alone (first lane) did not pull CcrZ down (3<sup>rd</sup> lane). **d**,  
940 FtsZ from *S. pneumoniae* expressed in *E. coli* co-purifies with CcrZ<sub>Sp</sub>-GFP by affinity purification.  
941 WC: whole cell extract, S: supernatant, HE: heat eluted products, C: CcrZ-GFP, F: FtsZ. **e**,  
942 Epifluorescence time-lapse microscopy of CcrZ-mKate2 at 37°C in presence (left panel) or absence  
943 (right panel) of FtsZ. When FtsZ amounts are reduced, cells increase their size and CcrZ is de-  
944 localized from mid-cell.

945

#### 946 **Fig. 4: CcrZ-depleted cells under-replicate**

947 **a**, Time-lapse microscopy of HlpA-mKate2 at 30°C in a  $\Delta ccrZ$  mutant shows several cells with  
948 defective DNA content. Orange arrows indicate a cell with no nucleoid after cell division; white  
949 arrows indicate a cell with “guillotined” DNA. **b**, Co-localization of FtsZ-CFP and HlpA-mKate2  
950 when depleting *ccrZ* indicates that several cells have a nucleoid located only on one side of the Z-  
951 ring. **c**, Three isolated *ccrZ* mutants (*ccrZ*<sup>supp1-3</sup>) restore wild type growth to  $\Delta ccrZ$ . **d**, DAPI staining  
952 of the three selected *ccrZ* suppressors mutants shows a restoration of DNA content. **e**, Schematic  
953 representation of the localization of suppressor mutations in the domain III of DnaA and in the  
954 DnaA/DnaN binding motif (ANB) of YabA. TM: tetramerization domain. **f**, *oriC/ter* ratios as  
955 determined by RT qPCR for D39V wild type and *ccrZ* depleted cells. Average values are indicated  
956 under the boxes. *ccrZ* depletion leads to a clear reduction in *oriC/ter* ratio. See Methods for statistical  
957 tests. **g**, *oriC/ter* ratios for *S. aureus* upon *ccrZ*<sub>Sa</sub> depletion (left) and for *B. subtilis* with *ccrZ*<sub>Bs</sub>  
958 deletion (right). **h**, *oriC/ter* ratios of strains with *dnaA* mutations re-inserted into a  $\Delta ccrZ$  background

959 show that these mutations restore replication initiation rates. **i**, *yabA* deletion leads to an increase in  
960 *oriC/ter* ratios, while suppressor mutation *ccrZ<sup>supp3</sup>* ( $\Delta ccrZ$ , *yabA-E93\**) as well as co-deletion of *yabA*  
961 together with *ccrZ* ( $\Delta yabA \Delta ccrZ$ ) restore a wild type ratio. **j**, While *yabA* deletion alters the growth  
962 rate, a  $\Delta yabA \Delta ccrZ$  double mutant grows like wild type. *dnaA Q247H* and *dnaA S292G* mutation  
963 also restore a wild type rate in a  $\Delta ccrZ$  mutant. **k**, *dnaA* mutation in a wildtype background increases  
964 the *oriC/ter* ratios. **l**, Schematic overview of CRISPRi-seq. *ccrZ*-depletion strain (*ccrZ<sup>-/+</sup>*) was  
965 transformed with 1,499 different sgRNAs targeting 2,111 genetic elements of *S. pneumoniae*. These  
966 sgRNAs are expressed constitutively. The resulting library is then grown in presence or absence of  
967 inducer for production of dCas9 and the genomic DNA isolated. After sequencing of the sgRNA  
968 region, reads counts are compared between *ccrZ* depleted induced and complemented induced,  
969 indicating which sgRNAs were enriched or deprived. This fold change directly informs whether the  
970 gene targeted by the sgRNA becomes more (beneficial) or less (detrimental) essential in a specific  
971 genetic background. **m**, CRISPRi-seq of *ccrZ*-depletion vs *ccrZ*-expression shows a positive  
972 interaction between *ccrZ* and *yabA / holB* (these two genes are in the same operon) and a negative  
973 interaction between *ccrZ* and *ftsK / rocS*. **n**, *oriC/ter* ratios for FtsZ depletion strain (*FtsZ<sup>-/+</sup>*) shows a  
974 reduced ratio when FtsZ is depleted (- IPTG) compared to when it is complemented (+ IPTG).

975

## 976 **Fig. 5: CcrZ activates DnaA-dependent replication initiation**

977 **a**, Localization of FtsZ-mTurquoise2 in a thermo-sensitive DnaA strain (*dnaA<sup>TS</sup>*) at permissive (30°C)  
978 and non-permissive (40°C) temperatures shows that *dnaA* inactivation leads to a similar phenotype as  
979 *ccrZ* inactivation. **b**, TEM of DnaA<sup>TS</sup> at non-permissive temperature (40°C) indicates the presence of  
980 multiple septa, similarly to a  $\Delta ccrZ$  mutant. **c**, When replication is driven in a RepN-dependent  
981 manner in *B. subtilis* (*oriN*), no decrease in *ori/ter* ratio can be observed in absence of *ccrZ<sub>Bs</sub>* (*oriN*,  
982  $\Delta ccrZ<sub>Bs</sub>$ ). **d**, Schematic representation of CcrZ motifs. CcrZ has one putative domain annotated APH  
983 (Phosphotransferase enzyme family; PFAM01636). Sequence alignment with several kinases revealed  
984 the presence of a conserved P-loop, APH and Brenner's motifs, found in most phosphotransferases.  
985 Locations of mutations made for 3 essential (red) and 2 non-essential (black) conserved residues are  
986 shown underneath. **e**, LicA choline kinase structure complexed with AMP and MES (2-(N-

987 morpholino)ethanesulfonic acid). The 5 residues indicated in yellow are conserved between CcrZ and  
988 LicA (and highly conserved within Firmicutes). **f**, Mutation of three of these five conserved residues  
989 in the putative ATP binding pocket leads to growth defects. **g**, Localization of CcrZ- H157A-GFP and  
990 CcrZ-D177A-GFP is not impaired.

991

992 **Fig. 6: Spatio-temporal localization of CcrZ via FtsZ ensures proper timing of DNA replication**  
993 **in *S. pneumoniae***

994 **a**, Microscopy of the origin of replication (yellow), replication fork (cyan) and CcrZ (red) in live *S.*  
995 *pneumoniae* wild type background cells. **b**, DnaN, *oriC* and CcrZ localizations grouped by cell area  
996 ( $\mu\text{m}^2$ ) in five equally sized groups. Analyzed from snapshots of exponentially growing cells. **c**,  
997 Single-cell kymographs of DnaN, CcrZ and *oriC* localizations in a 2:30 minute interval time-lapse  
998 movie. **d**, Tracked DnaN, *oriC* and CcrZ over time in a single cell. Top: overlay of fluorescence, cell  
999 outline and phase-contrast of the cell displayed in panel c and bottom: fluorescence localization on the  
1000 length axis of the same single cell over time. **e**, Model for spatio-temporal control of replication by  
1001 CcrZ. In *S. pneumoniae*, CcrZ is brought to the middle of the cell where the DnaA-bound origin of  
1002 replication is already positioned. CcrZ then stimulates DnaA to trigger DNA replication by an as of  
1003 yet unknown activity, possibly involving a phosphor-transfer event. While the precise regulation and  
1004 localization of CcrZ seems diverse between different organisms, CcrZ's activity to stimulate DNA  
1005 replication is conserved, at least in *S. pneumoniae*, *S. aureus* and *B. subtilis*.

1006

1007 **Extended Data**

1008 **Extended Data Fig. 1. *ccrZ* deletion phenotype is conserved in *S. aureus*.**

1009 **a**, Left: CcrZ conservation in firmicutes. Percentages indicate the highest percent identity, for each  
1010 class, obtained using PSI-BLAST with NIH sequences. Right: genes co-occurrence in several  
1011 genomes (data obtained from <https://string-db.org>; see Supplementary methods). Horizontal section  
1012 indicate complexity in neighborhood score assignment; white triangles indicate missing annotation. **b**,  
1013 Growth curves at 37°C and 30°C of *ccrZ* depletion mutants using  $P_{lac}$  (left) or  $P_{Zn}$  (right). **c**, Western  
1014 blot from different pneumococcal strains. C: native CcrZ size; X: unknown protein recognized by  $\alpha$ -

1015 *ccrZ* IgG. **d**, Microscopy of DAPI-stained *S. aureus* upon *ccrZ* silencing shows anucleate cells, while  
1016 *B. subtilis*  $\Delta ccrZ$  mutant did not present nucleoid defects. However,  $\Delta ccrZ$  <sub>Sa</sub> cells were longer (or less  
1017 well separated) and thinner (top right; wild type: 483 cells,  $\Delta ccrZ$  <sub>Bs</sub> 399 cells; each dot represents a  
1018 measurement) \*\*\*: *p*-value <0.001 Wilcoxon rank sum test. Bottom-left: chromosome defects upon  
1019 *ccrZ* <sub>Sa</sub> silencing can be rescued by expression of *ccrZ* <sub>Bs</sub> (*ccrZ* <sub>Sa</sub> <sup>sgRNA</sup>-*P* <sub>ccrZSa</sub>-*ccrZ* <sub>Bs</sub> + IPTG). Associated  
1020 growth curves (bottom-right) also confirmed the complementation of *ccrZ* <sub>Sa</sub> by *ccrZ* <sub>Bs</sub>. **e**,  
1021 Immunostaining of the polysaccharide capsule of *S. pneumoniae* wild type and upon *ccrZ* depletion.

1022

1023 **Extended Data Fig. 2. Septal localization of CcrZ in *S. pneumoniae*.**

1024 **a**, Immunostaining of CcrZ in wild type *S. pneumoniae* shows a septal localization. **b**, Localization of  
1025 CcrZ in other pneumococcal strains (un-encapsulated R6 strain and capsular serotype 4 TIGR4) and  
1026 in *S. aureus* SH1000, as well as in *B. subtilis* 1A700. **c**, 3D-SIM of GFP-CcrZ (green) and FtsZ-  
1027 mCherry (red) and reconstructed volume projection of both.

1028

1029 **Extended Data Fig. 3. Deletion of *ccrZ* leads to anucleate cells.**

1030 **a**, Localization of the nucleoid associated protein HlpA in a *ccrZ* mutant shows anucleate cells. **b**,  
1031 Mapping of DnaA Q247 and S292 residues onto the crystal structure of DnaA's AAA+ and duplex-  
1032 DNA-binding domains from *Aquifex aeolicus*. Both residues are predicted to be in the AAA+ domain.  
1033 DnaA Q247 and S292 correspond to *A. aeolicus* DnaA Q208 and E252 respectively.

1034

1035 **Extended Data Fig. 4. CcrZ activity is crucial for proper replication initiation as a *dnaA*<sup>TS</sup>**  
1036 **mutant phenocopied a *ccrZ* deletion.**

1037 **a**, Microscopy of DAPI-stained DnaA thermosensitive strain at non-permissive temperature (40°C)  
1038 indicates several anucleate cells, compared to a wild type grown in identical conditions. **b**, No  
1039 interaction was detected between DnaA and CcrZ using bacterial-2-hybrid, while a positive DnaA-  
1040 DnaA self-interaction is visible. **c**, Using split-luc assay, no interaction between CcrZ-YabA was  
1041 detected, while a strong signal was obtained for DnaA-YabA. DnaA level was controlled by P<sub>lac</sub> to  
1042 avoid toxicity. Each circle represents the average of 15 measurements of a technical replicate, with the



1043 size of the dot representing the SEM. **d**, Five (H157, D159, N164, D177 and D189) most conserved  
1044 residues between 1000 different CcrZ sequences from different bacterial species; sequences obtained  
1045 from UniRef50 database.

1046

1047 **Extended Data Fig. 5. Transient co-localization of CcrZ and DnaA.**

1048 Co-localization of CcrZ-mKate2 with DnaA-GFP (left) and corresponding heatmap of signal  
1049 distribution over cell length (right) show that DnaA and CcrZ co-localize at the beginning of the cell  
1050 cycle.

1051

1052 **Supplementary information**

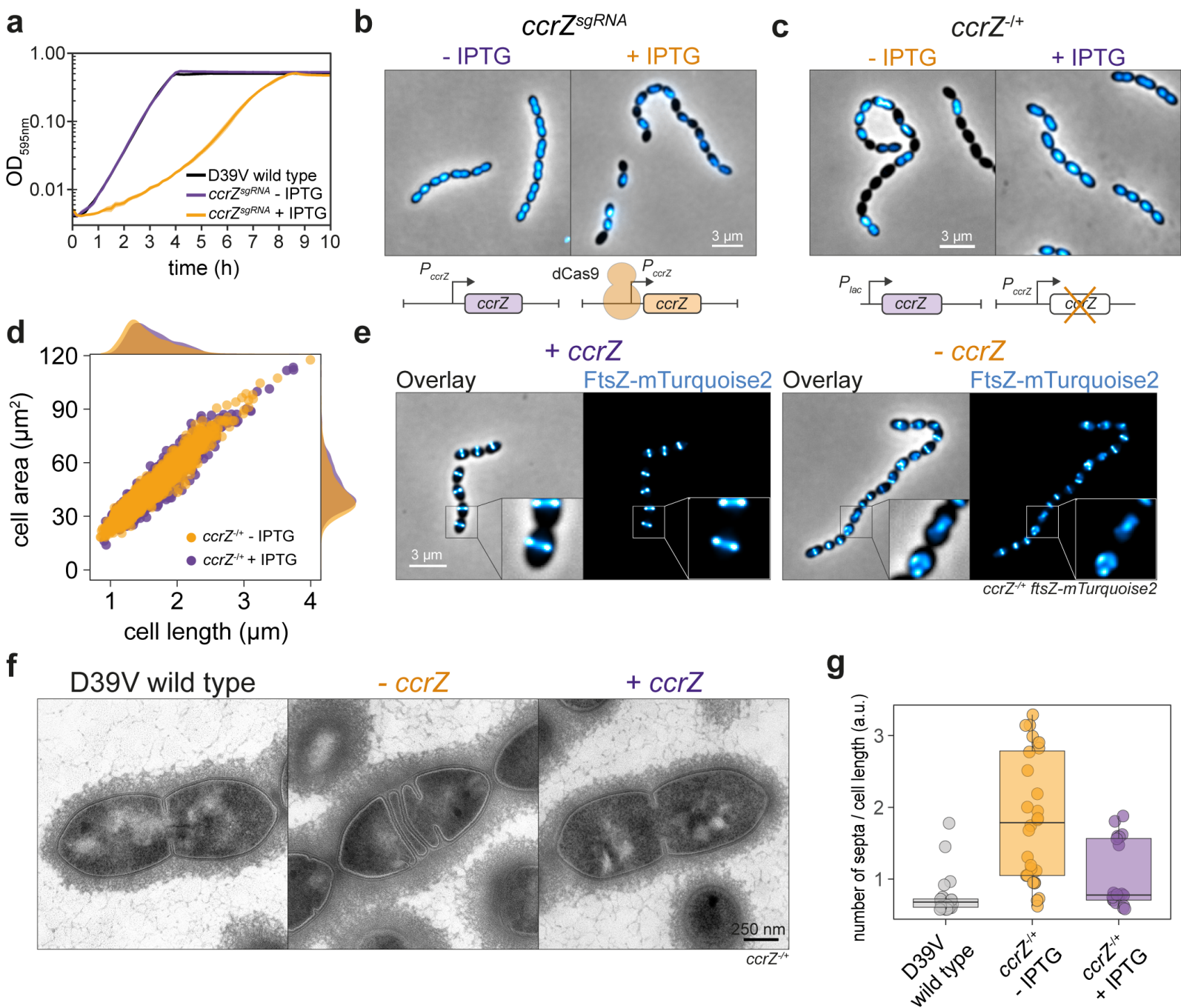
1053 Supplementary Videos legends, Supplementary Methods, Supplementary Tables 1-3, and

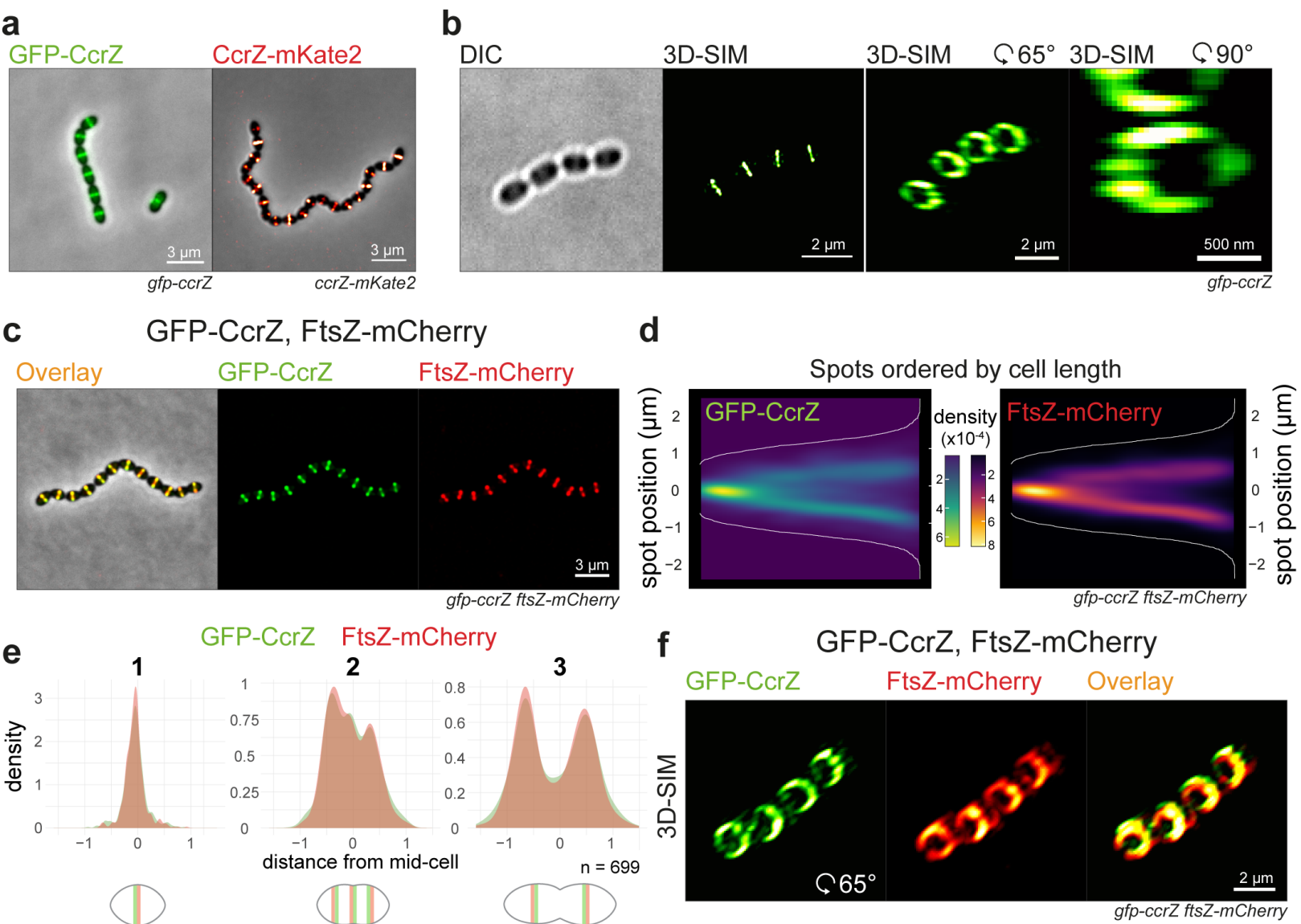
1054 Supplementary References.

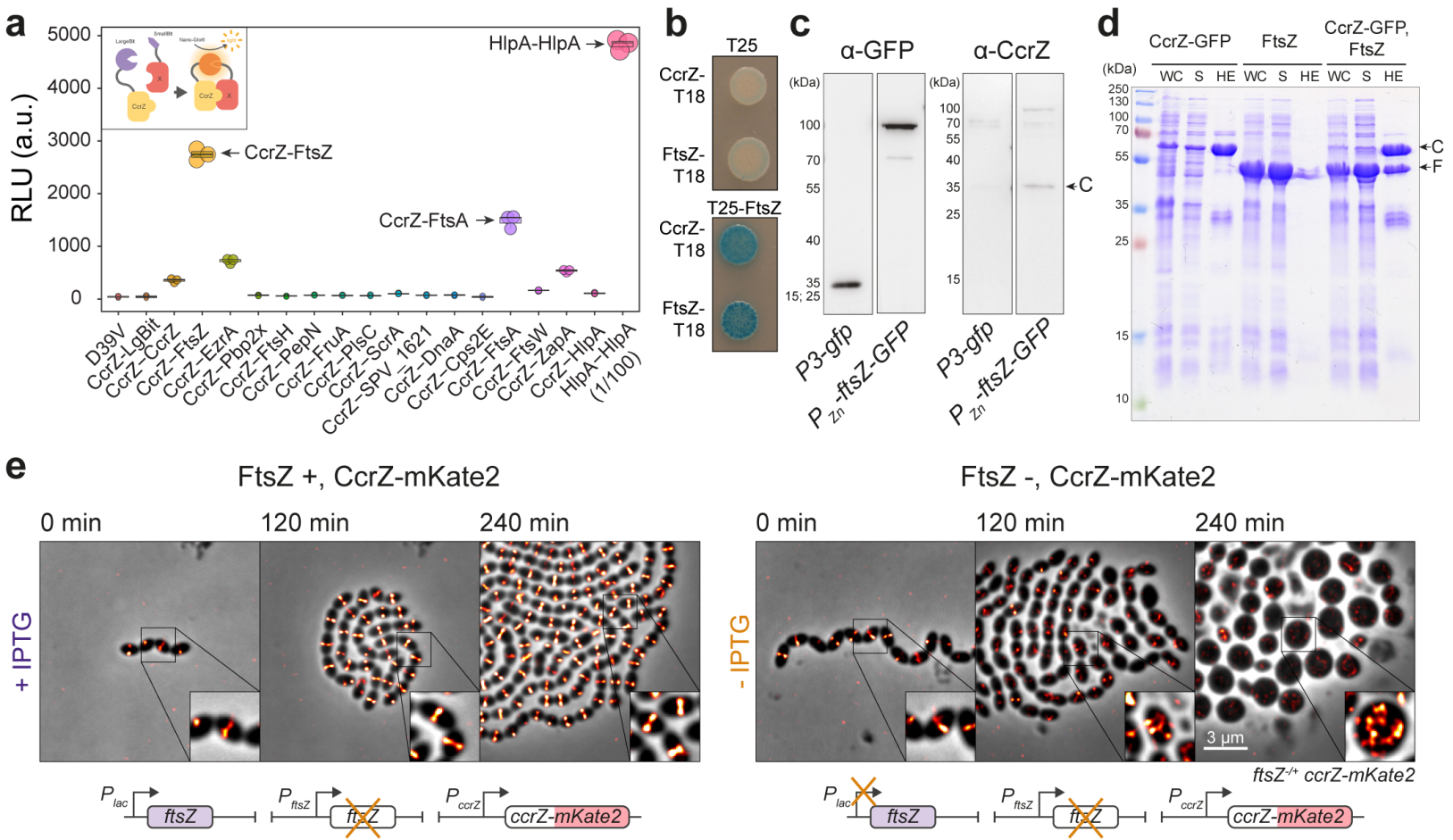
1055

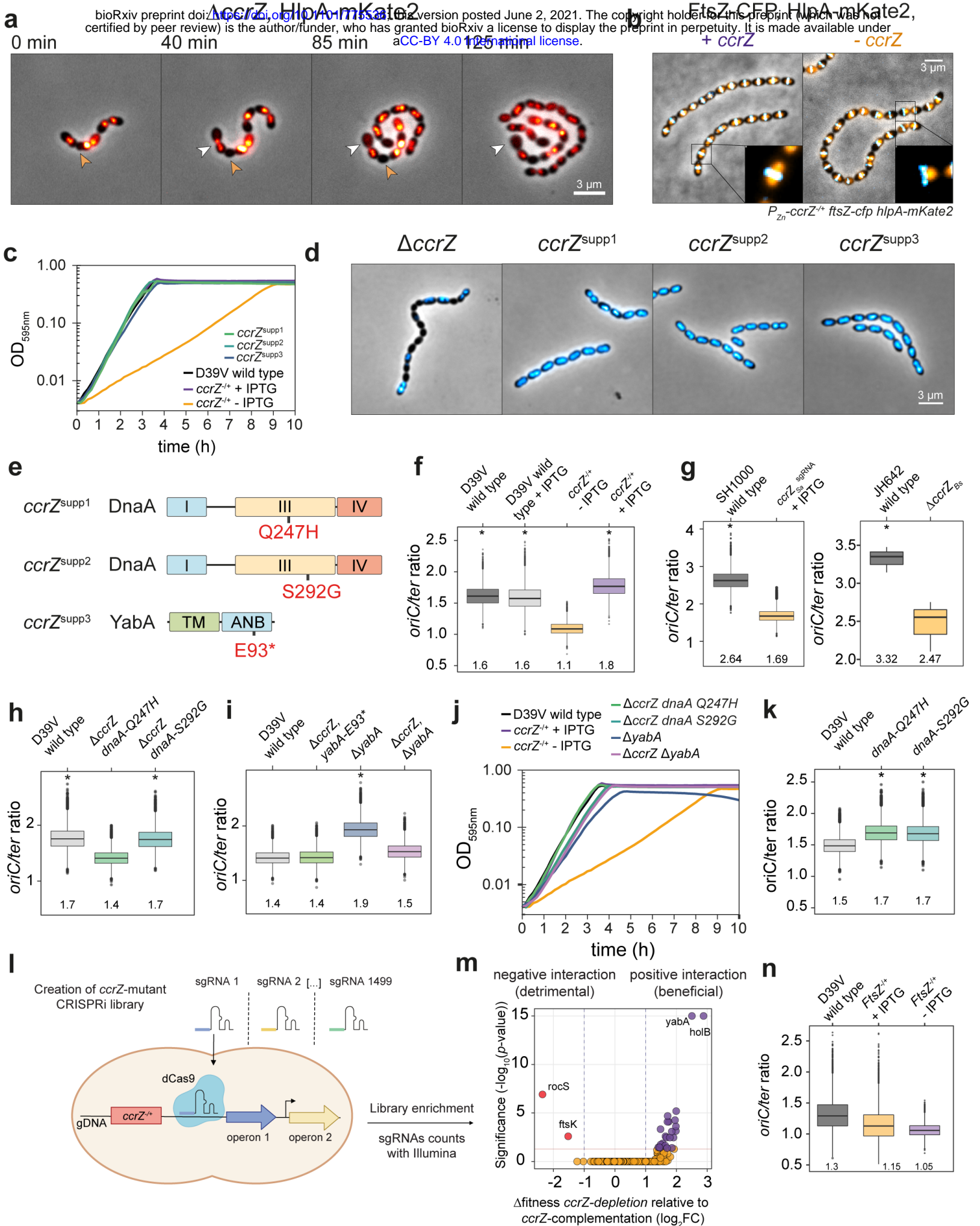
1056 **Supplementary Table 4**

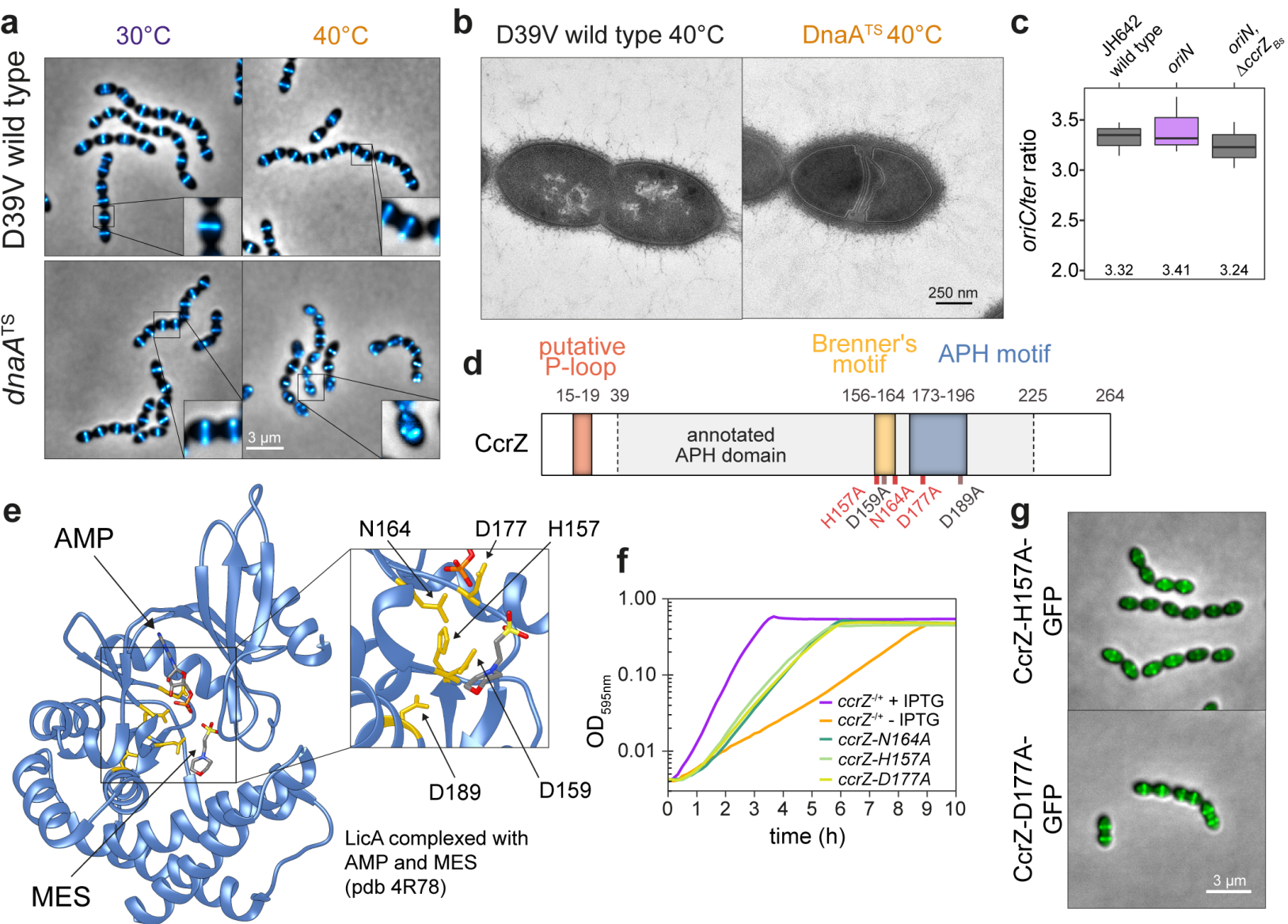
1057 CRISPRi-seq results for ccrZ-complementation vs ccrZ-depletion



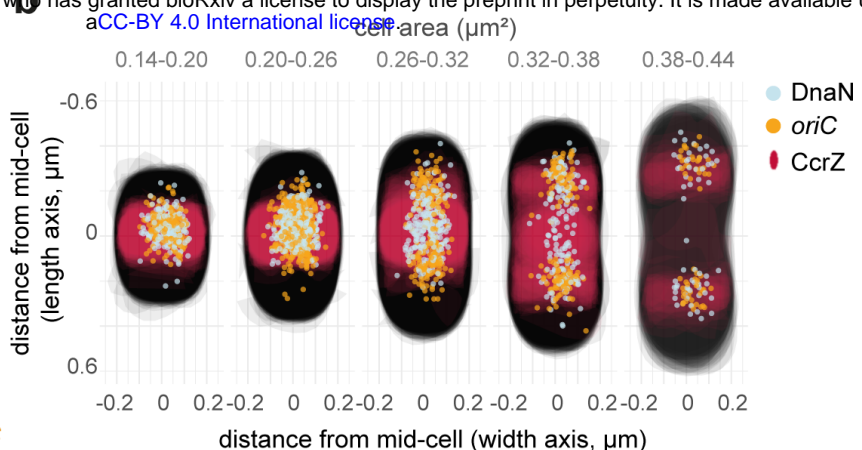
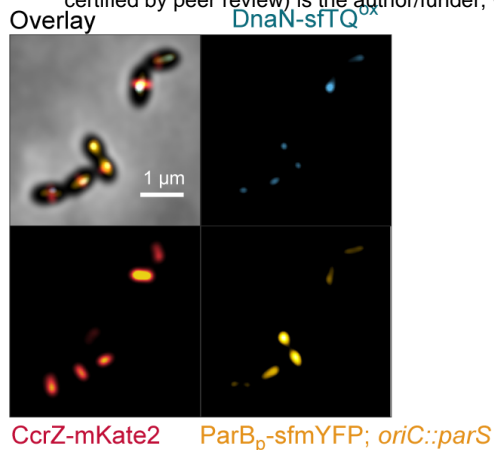




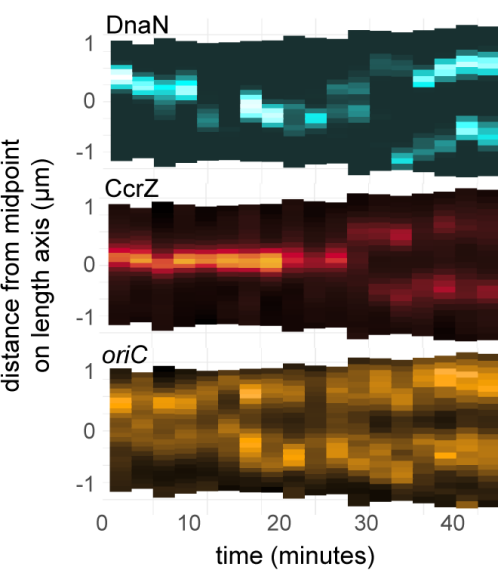




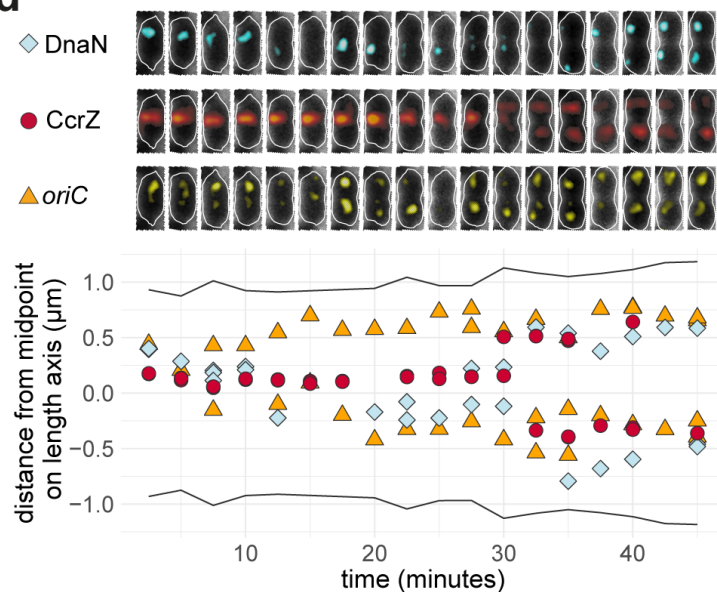
**a**



**c**

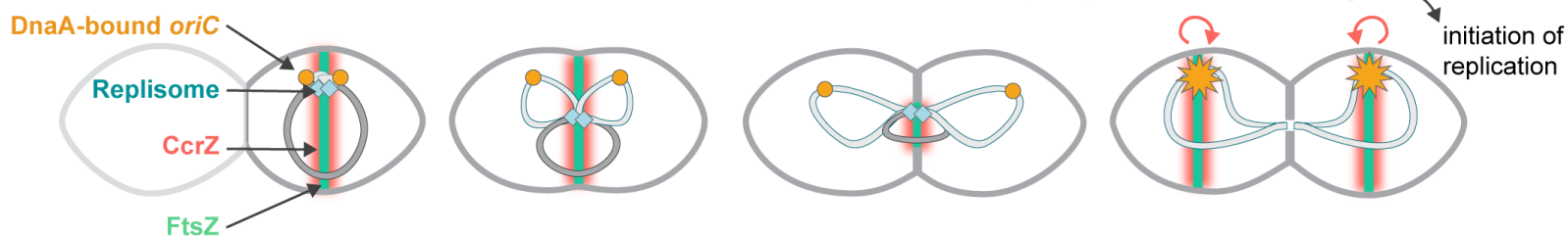


**d**



**e**

D39V wild type



$\Delta ccrZ$

